A&A 582, A28 (2015)
DOI: 10.1051/0004-6361/201424643

Astronomy & Astrophysics

Planck intermediate results

XXV. The Andromeda galaxy as seen by *Planck*

Planck Collaboration: P. A. R. Ade[82], N. Aghanim[55], M. Arnaud[69], M. Ashdown[65,6], J. Aumont[55], C. Baccigalupi[81], A. J. Banday[90,10], R. B. Barreiro[61], N. Bartolo[28,62], E. Battaner[91,92], R. Battye[64], K. Benabed[56,89], G. J. Bendo[88], A. Benoit-Lévy[22,56,89], J.-P. Bernard[90,10], M. Bersanelli[31,48], P. Bielewicz[78,10,81], A. Bonaldi[64], L. Bonavera[61], J. R. Bond[9], J. Borrill[13,84], F. R. Bouchet[56,83], C. Burigana[47,29,49], R. C. Butler[47], E. Calabrese[87], J.-F. Cardoso[70,1,56], A. Catalano[71,68], A. Chamballu[69,14,55], R.-R. Chary[53], X. Chen[53], H. C. Chiang[25,7], P. R. Christensen[79,34], D. L. Clements[52], L. P. L. Colombo[21,63], C. Combet[71], F. Couchot[67], A. Coulais[68], B. P. Crill[63,11], A. Curto[61,6,65], F. Cuttaia[47], L. Danese[81], R. D. Davies[64], R. J. Davis[64], P. de Bernardis[30], A. de Rosa[47], G. de Zotti[44,81], J. Delabrouille[1], C. Dickinson[64], J. M. Diego[61], H. Dole[55,54], S. Donzelli[48], O. Doré[63,11], M. Douspis[55], A. Ducout[56,52], X. Dupac[36], G. Efstathiou[58], F. Elsner[22,56,89], T. A. Enßlin[75], H. K. Eriksen[59], F. Finelli[47,49], O. Forni[90,10], M. Frailis[46], A. A. Fraisse[25], E. Franceschi[47], A. Frejsel[79], S. Galeotta[46], K. Ganga[1], M. Giard[90,10], Y. Giraud-Héraud[1], E. Gjerløw[59], J. González-Nuevo[18,61], K. M. Górski[63,93], A. Gregorio[32,46,51], A. Gruppuso[47], F. K. Hansen[59], D. Hanson[76,63,9], D. L. Harrison[58,65], S. Henrot-Versillé[67], C. Hernández-Monteagudo[12,75], D. Herranz[61], S. R. Hildebrandt[63,11], E. Hivon[56,89], M. Hobson[6], W. A. Holmes[63], A. Hornstrup[15], W. Hovest[75], K. M. Huffenberger[23], G. Hurier[55], F. P. Israel[86], A. H. Jaffe[52], T. R. Jaffe[90,10], W. C. Jones[25], M. Juvela[24], E. Keihänen[24], R. Keskitalo[13], T. S. Kisner[73], R. Kneissl[35,8], J. Knoche[75], M. Kunz[16,55,3], H. Kurki-Suonio[24,42], G. Lagache[5,55], A. Lähteenmäki[2,42], J.-M. Lamarre[68], A. Lasenby[6,65], M. Lattanzi[29], C. R. Lawrence[63], R. Leonardi[36], F. Levrier[68], M. Liguori[28,62], P. B. Lilje[59], M. Linden-Vørnle[15], M. López-Caniego[36,61], P. M. Lubin[26], J. F. Macías-Pérez[71], S. Madden[69], B. Maffei[64], D. Maino[31,48], N. Mandolesi[47,29], M. Maris[46], P. G. Martin[9], E. Martínez-González[61], S. Masi[30], S. Matarrese[28,62,39], P. Mazzotta[33], L. Mendes[36], A. Mennella[31,48], M. Migliaccio[58,65], M.-A. Miville-Deschênes[55,9], A. Moneti[56], L. Montier[90,10], G. Morgante[47], D. Mortlock[52], D. Munshi[82], J. A. Murphy[77], P. Naselsky[79,34], F. Nati[25], P. Natoli[29,4,47], H. U. Nørgaard-Nielsen[15], F. Noviello[64], D. Novikov[74], I. Novikov[79,74], C. A. Oxborrow[15], L. Pagano[30,50], F. Pajot[55], R. Paladini[53], D. Paoletti[47,49], B. Partridge[41], F. Pasian[46], T. J. Pearson[11,53], M. Peel[64,⋆], O. Perdereau[67], F. Perrotta[81], V. Pettorino[40], F. Piacentini[30], M. Piat[1], E. Pierpaoli[21], D. Pietrobon[63], S. Plaszczynski[67], E. Pointecouteau[90,10], G. Polenta[4,45], L. Popa[57], G. W. Pratt[69], S. Prunet[56,89], J.-L. Puget[55], J. P. Rachen[19,75], M. Reinecke[75], M. Remazeilles[64,55,1], C. Renault[71], S. Ricciardi[47], I. Ristorcelli[90,10], G. Rocha[63,11], C. Rosset[1], M. Rossetti[31,48], G. Roudier[1,68,63], J. A. Rubiño-Martín[60,17], B. Rusholme[53], M. Sandri[47], G. Savini[80], D. Scott[20], L. D. Spencer[82], V. Stolyarov[6,85,66], R. Sudiwala[82], D. Sutton[58,65], A.-S. Suur-Uski[24,42], J.-F. Sygnet[56], J. A. Tauber[37], L. Terenzi[38,47], L. Toffolatti[18,61,47], M. Tomasi[31,48], M. Tristram[67], M. Tucci[16], G. Umana[43], L. Valenziano[47], J. Valiviita[24,42], B. Van Tent[72], P. Vielva[61], F. Villa[47], L. A. Wade[63], B. D. Wandelt[56,89,27], R. Watson[64], I. K. Wehus[63], D. Yvon[14], A. Zacchei[46], and A. Zonca[26]

(Affiliations can be found after the references)

Received 21 July 2014 / Accepted 5 September 2015

ABSTRACT

The Andromeda galaxy (M 31) is one of a few galaxies that has sufficient angular size on the sky to be resolved by the *Planck* satellite. *Planck* has detected M 31 in all of its frequency bands, and has mapped out the dust emission with the High Frequency Instrument, clearly resolving multiple spiral arms and sub-features. We examine the morphology of this long-wavelength dust emission as seen by *Planck*, including a study of its outermost spiral arms, and investigate the dust heating mechanism across M 31. We find that dust dominating the longer wavelength emission ($\gtrsim$0.3 mm) is heated by the diffuse stellar population (as traced by 3.6 μm emission), with the dust dominating the shorter wavelength emission heated by a mix of the old stellar population and star-forming regions (as traced by 24 μm emission). We also fit spectral energy distributions for individual 5′ pixels and quantify the dust properties across the galaxy, taking into account these different heating mechanisms, finding that there is a linear decrease in temperature with galactocentric distance for dust heated by the old stellar population, as would be expected, with temperatures ranging from around 22 K in the nucleus to 14 K outside of the 10 kpc ring. Finally, we measure the integrated spectrum of the whole galaxy, which we find to be well-fitted with a global dust temperature of (18.2 ± 1.0) K with a spectral index of 1.62 ± 0.11 (assuming a single modified blackbody), and a significant amount of free-free emission at intermediate frequencies of 20–60 GHz, which corresponds to a star formation rate of around 0.12 $M_\odot\,\mathrm{yr}^{-1}$. We find a 2.3$\sigma$ detection of the presence of spinning dust emission, with a 30 GHz amplitude of 0.7 ± 0.3 Jy, which is in line with expectations from our Galaxy.

Key words. galaxies: individual: Messier 31 – galaxies: structure – galaxies: ISM – submillimeter: galaxies – radio continuum: galaxies

⋆ Corresponding author: M. Peel, email@mikepeel.net

1. Introduction

The infrared (IR) and submillimetre (submm) wavelength domain is particularly useful for understanding the processes driving star formation in various galactic environments, since dust grains re-emit in this frequency window the energy that has been absorbed from the UV-optical starlight. Our view of the global inner and outer disk star formation and ISM properties of the spiral galaxy in which we live is limited by our position inside the Galaxy, but our nearest spiral neighbour, the Andromeda galaxy (also known as Messier 31), offers the best view of the environmental effects within an entire galaxy, particularly because of its large angular extent on the sky.

M 31 has been extensively studied at IR/submm wavelengths with data from the Infrared Astronomical Satellite (IRAS, Habing et al. 1984; Walterbos & Schwering 1987), the Infrared Space Observatory (ISO, Haas et al. 1998), the *Spitzer* Space Telescope (Barmby et al. 2006; Gordon et al. 2006; Tabatabaei & Berkhuijsen 2010), and, most recently, the *Herschel* Space Observatory (Fritz et al. 2012; Groves et al. 2012; Smith et al. 2012; Ford et al. 2013; Draine et al. 2014; Viaene et al. 2014; Kirk et al. 2015). Except for the *Herschel* data, these IR observations have been restricted to observing the peak of the dust emission in the far infrared (FIR) as well as mid-infrared (MIR) emission from $\gtrsim$100 K dust and polycyclic aromatic hydrocarbons. In contrast, due to the large angular size of M 31 it has been particularly difficult to map the entire galaxy at wavelengths longer than 500 μm, which is needed to constrain the Rayleigh-Jeans side of the dust emission and the contribution of non-thermal emission sources to the spectral energy distribution (SED). In fact, the submm data for nearby spiral galaxies that have been published (e.g., Dunne et al. 2000; Stevens et al. 2005; Dale et al. 2007) have had low signal-to-noise levels, have been biased towards infrared-bright sources, or have only covered the centres of galaxies.

Data from *Planck* (Tauber et al. 2010)[1], which range from 28.4 to 857 GHz (10.5 to 0.35 mm) with angular resolution between 31′ and 5′, allow us to examine the Rayleigh-Jeans tail of the dust SED and the transition into free-free and synchrotron emission at longer wavelengths. Moreover, since *Planck* observed the entire sky at high sensitivity, its High Frequency Instrument (HFI, Lamarre et al. 2010) provides high signal-to-noise maps of M 31 that extend to the outermost edges of the galaxy.

Planck's large-scale map of the region provides the opportunity to study dust heating in M 31 out to the optical radius of the galaxy. Prior investigations with IRAS of dust heating in our Galaxy and others had produced seemingly contradictory results, with some studies indicating that dust seen at 60–100 μm was heated primarily by star-forming regions (Devereux & Young 1990; Buat & Xu 1996) and others demonstrating that evolved stellar populations could partially contribute to heating the dust seen by IRAS (e.g., Lonsdale Persson & Helou 1987; Walterbos & Schwering 1987; Sauvage & Thuan 1992; Walterbos & Greenawalt 1996). More recent observations with *Herschel* of a number of galaxies, including M 81, M 83, NGC 2403 (Bendo et al. 2010, 2012a) and M 33 (Boquien et al. 2011), demonstrated that dust-dominating emission at wavelengths shorter than 160 μm was primarily heated by star-forming regions (henceforth abbreviated as "SFR dust"), while dust-dominating emission at wavelengths over 250 μm may be primarily heated by the total stellar populations, including evolved stars in the discs and bulges of the galaxies (henceforth abbreviated as interstellar radiation field dust, or "ISRF dust". *Planck* observations of the SED of M 31 allow us to examine dust heating within the galaxy at frequencies much lower than was possible with *Herschel*. Once the dust heating sources are identified empirically and the SED is separated into different thermal components based on the heating sources, it will be possible to more accurately measure the temperature of the coldest dust within M 31, which is also critically important to properly estimate the dust mass.

Non-thermal emission from M 31 can also be measured at the lowest frequencies covered by *Planck*. Synchrotron emission from M 31 was discovered in the early days of radio astronomy (Brown & Hazard 1950, 1951). It has subsequently been mapped at low frequencies (Beck et al. 1998; Berkhuijsen et al. 2003), and associated emission has even been detected at gamma-ray frequencies (Abdo et al. 2010). However, the synchrotron emission has not been studied at higher frequency. Free-free emission is also expected from M 31. This emission may be used to measure star formation rates in a way that is not affected by dust extinction or reliant upon assumptions about the dust heating sources (e.g., see Murphy et al. 2011). Free-free emission from M 31 was first seen by Hoernes et al. (1998), as well as Berkhuijsen et al. (2003) and Tabatabaei et al. (2013). *Planck* data provide the opportunity to characterize the high-frequency radio emission for the first time.

Section 2 of this paper describes the *Planck* data, and Sect. 3 the ancillary data that we use here. We discuss the morphology of the dust as seen by *Planck* in Sect. 4, the colour ratios and the implications they have on the dust heating mechanism in Sect. 5, and the spectral energy distributions on 5′ scales in Sect. 6 and for the whole of M 31 in Sect. 7. We conclude in Sect. 8.

2. *Planck* data

Planck (Tauber et al. 2010; Planck Collaboration I 2011) is the third generation space mission to measure the anisotropy of the cosmic microwave background (CMB). It observes the sky in nine frequency bands covering 30–857 GHz (10.5 to 0.35 mm) with high sensitivity and angular resolution from 31′ to 5′. The Low Frequency Instrument (LFI; Mandolesi et al. 2010; Bersanelli et al. 2010; Mennella et al. 2011) covers the 30, 44, and 70 GHz (10.5, 6.8, and 4.3 mm) bands with amplifiers cooled to 20 K. The High Frequency Instrument (HFI; Lamarre et al. 2010; Planck HFI Core Team 2011a) covers the 100, 143, 217, 353, 545, and 857 GHz (3.0, 2.1, 1.38, 0.85, 0.55, and 0.35 mm) bands with bolometers cooled to 0.1 K. Polarization is measured in all but the highest two bands (Leahy et al. 2010; Rosset et al. 2010). A combination of radiative cooling and three mechanical coolers produces the temperatures needed for the detectors and optics (Planck Collaboration II 2011). Two data processing centres (DPCs) check and calibrate the data and make maps of the sky (Planck HFI Core Team 2011b; Zacchei et al. 2011). *Planck*'s sensitivity, angular resolution, and frequency coverage make it a powerful instrument for Galactic and extragalactic astrophysics as well as cosmology. Early astrophysics results are given in Planck Collaboration VIII–XXVI (2011), based on data taken between 13 August 2009 and 7 June 2010. Intermediate astrophysics results are presented in a series of papers between the major data releases.

[1] *Planck* (http://www.esa.int/Planck) is a project of the European Space Agency – ESA – with instruments provided by two scientific Consortia funded by ESA member states (in particular the lead countries: France and Italy) with contributions from NASA (USA), and telescope reflectors provided in a collaboration between ESA and a scientific Consortium led and funded by Denmark.

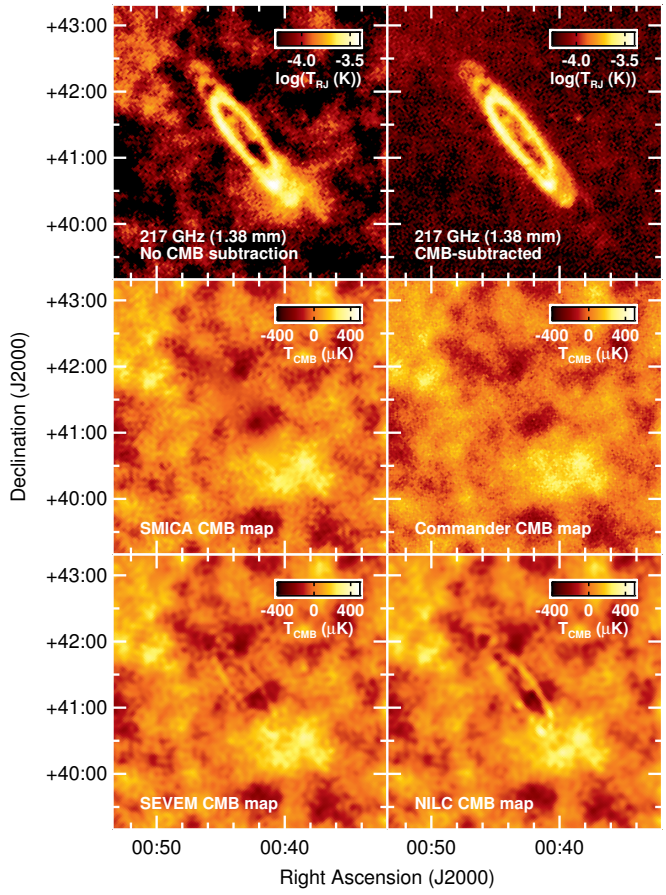

Fig. 1. *Top left*: M 31 at 217 GHz (1.38 mm), with no CMB subtraction. *Top right*: the SMICA CMB-subtracted 217 GHz (1.38 mm) map. *Middle left*: the SMICA map of the CMB in the same region. *Middle right*: Commander CMB map. *Bottom left*: SEVEM CMB map. *Bottom right*: NILC CMB map.

In this paper we use *Planck* data from the 2013 distribution of released products (Planck Collaboration I 2014), which can be accessed via the *Planck* Legacy Archive interface[2], based on the data acquired by *Planck* during its "nominal" operations period from 13 August 2009 to 27 November 2010. In order to study M 31 in the *Planck* maps, the CMB needs to be subtracted. CMB maps in the M 31 region are shown in Fig. 1. The CMB-subtracted *Planck* maps are presented in Fig. 2 at their native resolution and their properties are summarized in Table 1. We use various combinations of the *Planck* maps throughout this paper, and all maps are used to qualitatively study the emission at all *Planck* frequencies in Sect. 4. Maps at 217 GHz and higher frequencies (1.38 mm and shorter wavelengths) are used to quantitatively investigate the emission in Sects. 5 and 6, and all frequencies are used to measure the total emission in Sect. 7.

CMB subtraction is particularly important for M 31, given the similarities in angular size between M 31 and the anisotropies in the CMB. Additionally, there is an unfortunately large (approximately 290 μK) positive CMB fluctuation at the southern end of M 31, which can be clearly seen in the CMB map panels of Fig. 1. As part of the *Planck* 2013 delivery, CMB maps from four component separation techniques were released, namely maps from the Commander, NILC, SEVEM and SMICA component separation methods (Planck Collaboration XII 2014). We specifically use the SMICA CMB map to subtract the CMB from the *Planck* data, as from a visual inspection this appears to be the cleanest map of the CMB in this region from the four methods (see Fig. 1). The NILC and SEVEM maps are particularly contaminated by emission from M 31; we also use the NILC map to test the impact of residual foreground emission being subtracted out of the maps along with the CMB. Figure 1 shows the 217 GHz (1.38 mm) map pre- and post-CMB subtraction, along with the four CMB maps of the M 31 region.

The maps are converted from CMB temperature ($T_{\rm CMB}$) to Rayleigh-Jeans brightness temperature ($T_{\rm RJ}$) using the standard coefficients as described in Planck Collaboration (2013); we also use the nominal frequencies for the bands, and (when fitting a spectral model to the data) colour corrections, depending on the spectra of the emission. The 100 and 217 GHz (3.0 and 1.38 mm) *Planck* bands include CO emission. The CO emission from M 31 has been mapped with ground-based telescopes (e.g., Koper et al. 1991; Dame et al. 1993; Nieten et al. 2006), but these do not include the full extent of M 31 that is considered here. The CO emission is too weak to be reliably detected in the full-sky *Planck* CO maps (Planck Collaboration XIII 2014)[3]. We do not correct for the CO emission in the maps; instead we omit the 217 GHz (1.38 mm) channel from the SED fitting in Sect. 6, and we compare the level of CO emission expected from the ground-based CO map of Nieten et al. (2006) (described in Sect. 3.1) with the emission attributable to CO in the integrated *Planck* measurements of M 31 in Sect. 7.

To assess the uncertainty in the *Planck* maps, we estimate the instrumental noise and cirrus contamination by measuring the scatter of flux densities in an adjacent background region of the *Planck* maps (see Sect. 6 for details). We conservatively assume calibration uncertainties of 10% for 857 and 545 GHz (350 and 550 μm) and 3% for all other *Planck* frequencies (see Planck Collaboration 2013).

For the integrated spectrum analysis in Sect. 7, the *Planck* full-sky maps are used directly in HEALPix[4] format (Górski et al. 2005). For the higher resolution analyses, however, we use "postage stamp" 2D projected maps centred on M 31. To conserve the photometry of the data whilst repixelizing, we use the Gnomdrizz package (Paradis et al. 2012a) to create the postage stamp maps from the HEALPix data; since the HEALPix Gnomview function uses nearest-neighbour interpolation, it does not necessarily conserve the photometry, although we tested that there is no significant difference in this case. The resulting postage stamp maps in equatorial coordinates are of size $250' \times 250'$ with $0.5' \times 0.5'$ pixels, centred on RA $10\overset{\circ}{.}68$, Dec $41\overset{\circ}{.}27$ ($l = 121\overset{\circ}{.}2, b = -21\overset{\circ}{.}6$).

When quantitatively analysing the data, we first smooth to a common resolution of either $5'$ (at 217 GHz and above/1.38 mm or lower, where the data have a native resolution of $4.'39$–$4.'87$) or 1° (at all frequencies) by convolving the map with a circular Gaussian beam with a full-width at half-maximum (FWHM) of $\theta_{\rm conv} = \left(\theta^2_{\rm new} - \theta^2_{\rm old}\right)^{1/2}$, where $\theta_{\rm new}$ is the desired FWHM and $\theta_{\rm old}$ is the current FWHM of the maps. For some of the later analysis, we also repixelize the $5'$ resolution data into $5'$ pixels (see Sect. 5), while the 1° data are analysed at their native

[2] http://pla.esac.esa.int/pla/

[3] There is no detection in the *Planck* Type 1 CO map (Planck Collaboration XIII 2014); the morphology is not consistent with the known structure in the Type 2 map, and although there is a detection in the Type 3 map and the ring morphology is visible, the detection does not have a high signal-to-noise ratio and may be contaminated by dust emission.

[4] http://healpix.jpl.nasa.gov

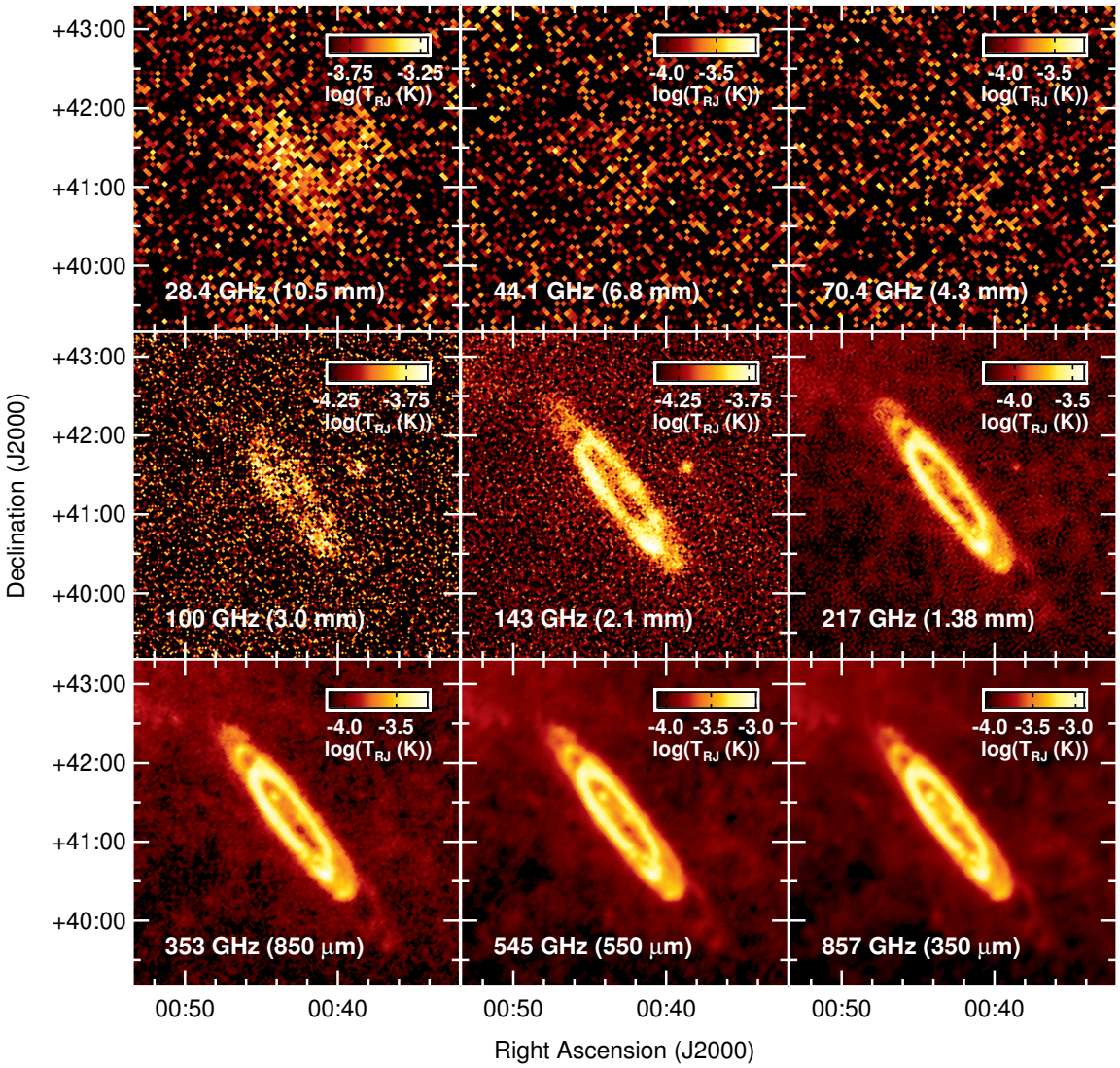

Fig. 2. Maps of M 31 in total intensity from *Planck* (after CMB subtraction). *Top to bottom, left to right*: *Planck* 28.4, 44.1, and 70.4 GHz; *Planck* 100, 143, and 217 GHz; *Planck* 353, 545, and 857 GHz. All plots have units of Kelvin ($T_{\rm RJ}$), have a 1° equatorial graticule overlaid, are 250′ × 250′ with 0.5′ × 0.5′ pixels and are centred on RA 10.°68, Dec 41.°27, with north up and east to the left.

`HEALPix` $N_{\rm side}$ resolution. The *Planck* beams are not symmetric at the roughly 20% level (e.g., see Zacchei et al. 2011; Planck HFI Core Team 2011b), and the ancillary data sets used (see Sect. 3) will also have non-Gaussian beams; smoothing the data to a common resolution reduces the effect of the asymmetry. However, a residual low-level effect will still be present in this analysis, for example in terms of introducing some correlation between adjacent 5′ pixels.

3. Ancillary data

The ancillary data that we use in this paper fall under two categories. For the higher resolution spatial analysis, we need observations with resolution equal to or greater than the *Planck* high frequency resolution of 5′; these are described in Sect. 3.1. For the integrated SED, we can make use of large-scale survey data with a resolution of 1° or higher; we describe these data sets in Sect. 3.2. All of the data sets are summarized in Table 1.

We also make use of ancillary information about the distance and inclination of M 31. M 31 is at a distance of (785 ± 25) kpc (McConnachie et al. 2005), with an optical major isophotal diameter of 190.′5 ± 0.′1 and a major-to-minor ratio of 3.09 ± 0.14 (de Vaucouleurs et al. 1991). Following Xu & Helou (1996), we assume that it has an inclination angle $i = 79°$ and a position angle of 37° with respect to North (both in equatorial coordinates).

3.1. The 5′ data set

We use six data sets in addition to the *Planck* data in our 5′ resolution study. At high frequencies, we use IRAS, *Spitzer*, *Herschel*, and ISO data to trace the shorter wavelength dust emission. At lower frequencies, we use ground-based H I and CO data sets to trace the gas within the galaxy. To match the pixelization and resolution of these other data to the *Planck* data, we regrid the data onto 0.25′ pixels in the same coordinate system and sky region as the *Planck* data and then smooth them to a common resolution of 5′. Further repixelization to 5′ pixels is then carried out for the analysis in later sections.

To trace dust emission in the infrared, we use 24, 70, and 160 μm data originally acquired by Gordon et al. (2006) using the Multiband Imaging Photometer for *Spitzer* (MIPS; Rieke et al. 2004) on the *Spitzer* Space Telescope (Werner et al. 2004).

Table 1. Sources of the data sets used in this paper, as well as their frequency, wavelength, resolution, calibration uncertainty, and rms on 5′ scales (for data with 5′ resolution or better only; see later).

Source	ν [GHz]	λ [mm]	Res.	Unc.	σ (5′, Jy)	Analysis	Reference
Haslam	0.408	734	60′	10%	...	L	Haslam et al. (1982)
Dwingeloo	0.820	365	72′	10%	...	L	Berkhuijsen (1972)
Reich	1.4	214	35′	10%	...	L	Reich et al. (2001)
WMAP 9-year	22.8	13	49′	3%	...	L	Bennett et al. (2013)
Planck	28.4	10.5	32′24	3%	...	L	Planck Collaboration II (2014)
WMAP 9-year	33.0	9.0	40′	3%	...	L	Bennett et al. (2013)
WMAP 9-year	40.7	7.4	31′	3%	...	L	Bennett et al. (2013)
Planck	44.1	6.8	27′01	3%	...	L	Planck Collaboration II (2014)
WMAP 9-year	60.7	4.9	21′	3%	...	L	Bennett et al. (2013)
Planck	70.4	4.3	13′25	3%	...	L	Planck Collaboration II (2014)
WMAP 9-year	93.5	3.2	13′	3%	...	L	Bennett et al. (2013)
Planck	100	3.0	9′65	3%	...	L	Planck Collaboration VI (2014)
Planck	143	2.1	7′25	3%	...	L	Planck Collaboration VI (2014)
Planck	217	1.38	4′99	3%	0.015	LH	Planck Collaboration VI (2014)
Planck	353	0.85	4′82	3%	0.05	LH	Planck Collaboration VI (2014)
Planck	545	0.55	4′68	7%	0.13	LH	Planck Collaboration VI (2014)
Herschel SPIRE PLW	600	0.50	0′59	4%	0.09	H	Fritz et al. (2012)
Planck	857	0.35	4′33	7%	0.31	LH	Planck Collaboration VI (2014)
Herschel SPIRE PMW	857	0.35	0′40	4%	0.23	H	Fritz et al. (2012)
Herschel SPIRE PSW	1200	0.25	0′29	4%	0.29	H	Fritz et al. (2012)
COBE-DIRBE	1249	0.240	40′	13%	...	L	Hauser et al. (1998)
ISO	1763	0.175	1′3	10%	0.8	H	Haas et al. (1998)
Spitzer MIPS B3	1870	0.16	0′63	12%	0.53	H	Gordon et al. (2006), Bendo et al. (2012b)
Herschel PACS	1874	0.16	0′22	4%	2.4	H	Fritz et al. (2012)
COBE-DIRBE	2141	0.14	40′	13%	...	L	Hauser et al. (1998)
COBE-DIRBE	2997	0.10	40′	13%	...	L	Hauser et al. (1998)
Herschel PACS	2998	0.10	0′21	4%	2.5	H	Fritz et al. (2012)
IRAS (IRIS) B4	3000	0.10	4′3	13%	0.37	LH	Miville-Deschênes & Lagache (2005)
Spitzer MIPS B2	4280	0.07	0′3	10%	0.12	H	Gordon et al. (2006), Bendo et al. (2012b)
COBE-DIRBE	5000	0.06	40′	13%	...	L	Hauser et al. (1998)
IRAS (IRIS) B3	5000	0.06	4′0	13%	0.12	LH	Miville-Deschênes & Lagache (2005)
IRAS (IRIS) B2	12 000	0.025	3′8	13%	0.06	LH	Miville-Deschênes & Lagache (2005)
Spitzer MIPS B1	12 490	0.024	0′1	4%	0.012	H	Gordon et al. (2006), Bendo et al. (2012b)
IRAS (IRIS) B1	25 000	0.012	3′8	13%	0.04	LH	Miville-Deschênes & Lagache (2005)
Spitzer IRAC	83 000	0.0036	1″7	3%	...	H	Barmby et al. (2006), Spitzer Science Center (2012)
DRAO H I	1.4	...	0′37	5%	...	H	Chemin et al. (2009)
IRAM CO	115.	...	0′38	15%	...	H	Nieten et al. (2006)

Notes. The Analysis column indicates whether the data set has been used in the 5′ high-resolution (H) and/or 1° low-resolution (L) analysis. The first part of the table describes the continuum data sets, and the second part describes the spectral line data sets.

The 24, 70, and 160 μm data have point spread functions with FWHM of 6″, 18″, and 38″, respectively. The data were processed using the MIPS Data Analysis Tools (Gordon et al. 2005) as well as additional data processing steps described by Bendo et al. (2012b). The data processing includes the removal of the effect of cosmic ray hits and drift in the background signal. The background is initially subtracted from the individual data frames by characterizing the variations in the background signal as a function of time using data that fall outside of the galaxy. This removes large-scale background/foreground structure outside the galaxy, including the cosmic infrared background (CIB) and zodiacal light, but residual foreground cirrus structures and compact sources remain in the data. Any residual background emission in the final maps is measured outside the optical disc of the galaxy and subtracted from the data. For additional details on the data reduction process, see the description of the data reduction by Bendo et al. (2012b). PSF characteristics and calibration uncertainties are described by Engelbracht et al. (2007), Gordon et al. (2007), and Stansberry et al. (2007). We use the data outside of the mask to assess the rms uncertainty in the *Spitzer* data, including thermal noise, residual cirrus and other large-scale features that contribute to the uncertainty on 5′ scales.

We additionally utilise the 3.6 μm data produced by Barmby et al. (2006) using the *Spitzer* Infrared Array Camera (IRAC; Fazio et al. 2004) to trace the older stellar population in the bulge of M 31; these data have a resolution of 1.″7.

We also include *Herschel* data from the *Herschel* Exploitation of Local Galaxy Andromeda (HELGA) survey (Fritz et al. 2012). These data are at 500, 350, 250, 160 and 100 μm (600, 857, 1200, 1874 and 2998 GHz) and have resolutions between 0.′21 and 0.′59 (Lutz 2012; Valtchanov 2014). We re-align the data to match the *Spitzer* 24 μm data using three compact sources that are seen at all *Herschel* frequencies. The *Herschel* data have a flux calibration uncertainty of 4% (*Herschel* Space Observatory 2013; Bendo et al. 2013). For the integrated SED, we smooth the *Herschel* data to 1°, and then regrid these data onto an oversampled $N_{\rm side}$ = 16 384 `HEALPix` map, which was then resampled down to $N_{\rm side}$ = 256.

We also make use of several data sets for comparison purposes, namely: the IRAS data at 12, 25, 60, and 100 μm from Miville-Deschênes & Lagache (2005); the ISO 175 μm data from Haas et al. (1998, priv. comm.); the H I emission map from Chemin et al. (2009); and the ^{12}CO $J = 1 \rightarrow 0$ map of M 31 from Nieten et al. (2006). These are described in Appendix A.

3.2. The 1° data set

When looking at the integrated spectrum of M 31, we make use of a number of large-area, low-resolution surveys. These are publicly available in `HEALPix` format. We convolve the data sets to a resolution of 1° to match the resolution of the low-frequency data sets and perform the analysis directly on the `HEALPix` maps.

At low frequencies, we use the low-resolution radio maps of the sky at 408 MHz (73.4 cm; Haslam et al. 1981, 1982), 820 MHz, (36.5 cm; Berkhuijsen 1972) and 1.4 GHz (21.4 cm; Reich 1982; Reich & Reich 1986; Reich et al. 2001). We assume that there is a 10% uncertainty in these maps, which includes both the uncertainty in the flux density calibration (between 5 and 10% depending on the survey) and also uncertainties arising from the morphology of the surrounding structure interacting with the aperture photometry technique we use. This choice of uncertainty has been shown to be reasonable for Galactic anomalous microwave emission (AME) clouds (Planck Collaboration Int. XV 2014). For the 408 MHz (73.4 cm) map, we also add 3.8 Jy to the uncertainty to take into account the baseline striations in the map, which are at the level of ±3 K (Haslam et al. 1982; Planck Collaboration Int. XV 2014). All of the maps have been calibrated on angular scales of around 5°, and consequently the difference between the main and full beams (the latter including sidelobes) needs to be taken into account when measuring the flux densities of more compact sources. This is significant for the 1.4 GHz (21.4 cm) map, where the factor for objects on 1° scales is approximately 1.55. As M 31 is on an intermediate scale, we adopt an intermediate correction factor of 1.3 ± 0.1, and also include the uncertainty in this correction factor in the flux density uncertainty. We assume that the value and uncertainty on the ratio for the 408 MHz (73.4 cm) and 820 MHz (36.5 cm) maps is small, and hence will be well within the existing calibration uncertainties, as per e.g., Planck Collaboration Int. XV (2014). We also make use of the integrated flux densities from higher-resolution surveys collated by Berkhuijsen et al. (2003) for comparison to those extracted from the maps.

At intermediate frequencies, in addition to *Planck*-LFI data, we use the deconvolved and symmetrized 1°-smoothed WMAP 9-year data at 22.8, 33.0, 40.7, 60.7, and 93.5 GHz (13, 9.0, 7.4, 4.9, and 3.2 mm; Bennett et al. 2013)[5]. When fitting a model to these data, we apply colour corrections following the recipe in Bennett et al. (2013), and we conservatively assume a calibration uncertainty of 3%.

At higher frequencies, we include the low-resolution COBE-DIRBE data at 1249, 2141, and 2997 GHz (240, 140, and 100 μm; Hauser et al. 1998), in addition to the IRAS data described in Appendix A. We assume that these data have an uncertainty of 13%. We also use the *Herschel* data as described above.

[5] http://lambda.gsfc.nasa.gov/product/map/dr4/maps_band_smth_r9_i_9yr_get.cfm

4. Infrared morphology

The *Planck* maps of M 31 are shown in Fig. 2. At 100 GHz and all higher *Planck* frequencies (3.0 mm and shorter wavelengths), the prominent 10 kpc dust ring of Andromeda can clearly be seen – as expected based on previous infrared observations of M 31 – as well as a number of other extended features.

At high frequencies, where we have the highest signal-to-noise and highest spatial resolution, we can see features much further out than the 10 kpc ring. The top panels of Fig. 3 show the *Planck* 857 GHz (350 μm) map labelled to show the locations of the key features in the dust emission; the bottom-left panel shows the *Herschel* 857 GHz (350 μm) data, and the bottom-right panel of Fig. 3 shows the H I map from Chemin et al. (2009) for comparison. A cut through the *Planck* 857 and 353 GHz (350 and 850 μm) maps is shown in Fig. 4. To the south, a total of four spiral arm or ring structures can clearly be seen – the 10 kpc ring ("F8"), as well as a second structure just outside of the ring ("F9") and the more distant 21 kpc ("F10") and 26 kpc ("F11") arms. These features have also been identified by Fritz et al. (2012), and can also be seen in the panel displaying the *Herschel* 857 GHz data. We see a hint of the emission at 31 kpc ("F12"), which is also seen in H I emission, but we are unable to confirm it as being part of M 31, because of the large amount of surrounding cirrus emission from our Galaxy. To the north, we see three sets of spiral arm structures ("F4", "F3", and "F2") and a wisp of emission at the northernmost end of the galaxy ("F1", confirmed by cross-checking against H I emission, as shown in the top-right panel) before running into confusion from Galactic emission. These features can be seen most clearly at 857 and 545 GHz (350 and 550 μm), but are also clearly visible in the 353, 217 and 143 GHz (0.85, 1.38 and 2.1 mm) maps after CMB subtraction. The 10 kpc ring can still be seen clearly at 100 GHz, but at that frequency the more extended structure is not visible. We will use the terminology of "ring" for the 10 kpc ring, since it has been clearly demonstrated to be a near-complete ring (e.g., see Haas et al. 1998), and "arm" for all other structures that may not completely circle the galaxy.

An area of particularly strong long-wavelength emission can be clearly seen at the southern end of the 10 kpc ring, down to frequencies of 100 GHz (3.0 mm; see Fig. 2; in Fig. 3 it is just to the right of "F8" and is also marked as "S6"). This has the highest contrast with the rest of M 31 at frequencies of 143 and 217 GHz (2.1 and 1.38 mm); there are also hints of it down to 70.4 GHz (4.3 mm). This is probably what is seen at the highest frequencies of the WMAP data and in *Planck* data by De Paolis et al. (2011, 2014); i.e., the asymmetrical emission between the north and south parts of M 31 that they detect is caused by either varying dust properties across the galaxy or CMB fluctuations, rather than being caused by galactic rotation.

Within the 10 kpc ring, several features are also visible. A bright spot inside the Galactic ring to the north is marked as "F5" in the top-right panel of Fig. 3. This region corresponds to a limb of an asymmetric spiral structure within the 10 kpc ring that has also been seen in the higher-resolution *Spitzer* data (Gordon et al. 2006). *Planck* does not detect the emission from the central nucleus, despite the prominence of this region in maps of M 31 at higher frequencies. This implies that the majority of the dust in this region is at a higher dust temperature than average – an implication which will be explored in later sections. *Planck* does, however, detect a compact object to the right of the nucleus (marked as "F7") that has also been seen with IRAS (Rice 1993), ISO (Haas et al. 1998), and *Spitzer* (Gordon et al. 2006);

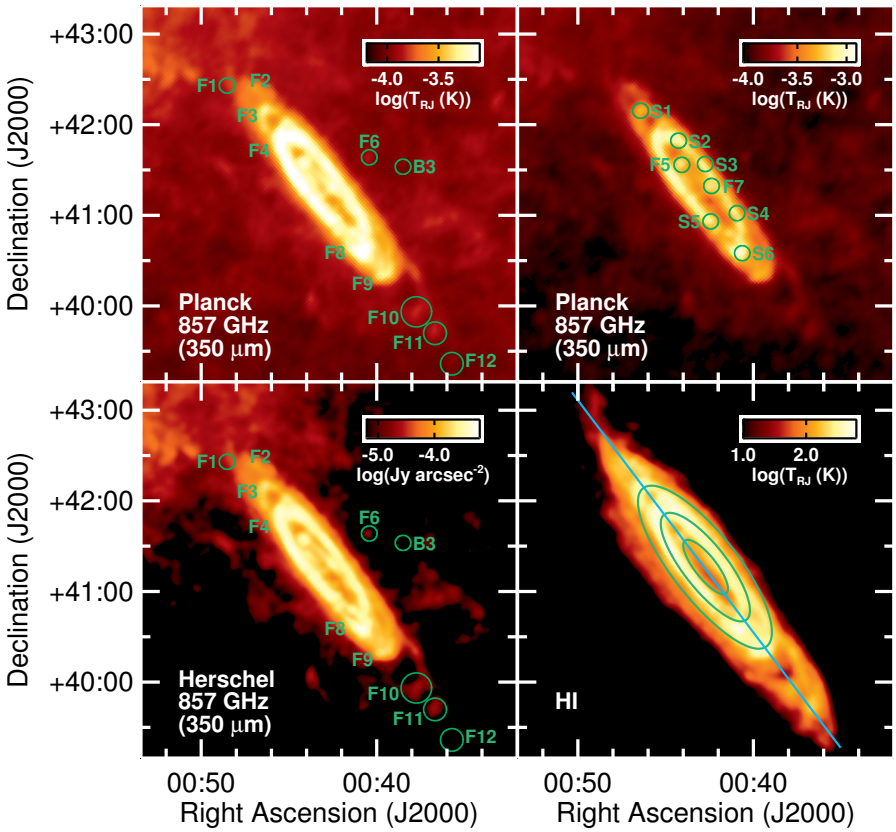

Fig. 3. *Top-left*: the 857 GHz (350 μm) *Planck* map of M 31, highlighting the extension of the dust out to large distances. Fields of interest are labelled with "F," and circled in some cases. The position of the radio source B3 0035+413 is also shown (labeled B3). *Top-right*: the 857 GHz (350 μm) map, with a scale chosen to highlight the brighter emission. Circles labelled with "S" indicate the sources included in the *Planck* ERCSC (see Appendix B); two fields in the centre region are also labelled with "F". *Bottom-left*: the 857 GHz (350 μm) *Herschel* map convolved to the same resolution as the *Planck* data, with the same fields of interest labelled as in the *Planck* map above. *Bottom-right*: a map of the H I emission from M 31 (Chemin et al. 2009) convolved to the same resolution as the *Planck* 857 GHz (350 μm) map, with 5, 10, and 15 kpc rings overlaid in green, and the cut used in Fig. 4 in blue.

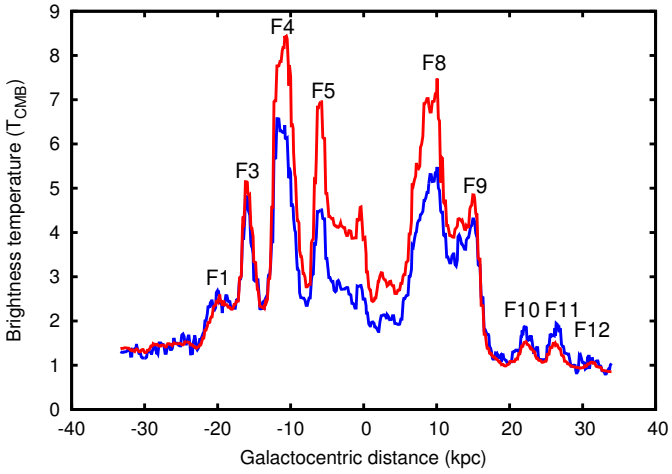

Fig. 4. Cut along the major axis of M 31. Negative values are on the higher declination side of the galaxy. The red line is 857 GHz (350 μm) and the blue line is 353 GHz (850 μm) rescaled by a factor of 1000. Various spiral arm structures, including the outermost rings at 20–30 kpc, are clearly visible at both frequencies. Fields are numbered as per Fig. 3.

the latter suggests that this emission is located where a bar and the spiral arm structure meet.

Outside of the ring, we see some cirrus dust emission from our own Galaxy, particularly at the higher *Planck* frequencies. This is largely present on the north side of M 31, towards the Galactic plane, but it can also be seen elsewhere, for example there is an arc of cirrus emission above the outermost rings at the south end of M 31. Depending on the temperature and spectral properties of this emission, it may present problems for studies of the Sunyaev-Zeldovich effect in the halo of M 31 (e.g., Taylor et al. 2003) unless the emission is properly taken into account or suitably masked.

At *Planck*'s lowest frequencies, M 31 is clearly detected but is not resolved, because of the low resolution at these frequencies. It is clearest at 28.4 GHz (10.5 mm), but can also be seen at 44.1 and 70.4 GHz (6.8 and 4.3 mm) – although at these frequencies CMB subtraction uncertainty starts to become important. The emission mechanism powering the source detections at these frequencies will be discussed in the context of the integrated SED in Sect. 7.

There are also several sources in the field near to M 31 that are present in the maps shown here, including the dwarf galaxy M110/NGC 205 ("F6") and the blazar B3 0035+413 ("B3"), additionally a number of components of M 31 are included in the *Planck* Early Release Compact Source Catalogue (ERCSC; Planck Collaboration VII 2011) and the *Planck* Catalogue of Compact Sources (PCCS; Planck Collaboration XXVIII 2014). We discuss these in Appendix B.

5. Colour ratios and implications for dust heating

5.1. Colour ratios

A number of recent analyses based on *Herschel* data have used FIR surface brightness ratios to examine dust heating sources within nearby galaxies. Bendo et al. (2010) performed the first such analysis on M 81; subsequent analyses were performed on M 33 by Boquien et al. (2011), on M 83 and NGC 2403 by Bendo et al. (2012a), and on a wider sample of galaxies by Bendo et al. (2015). These techniques have been shown to be more robust at identifying dust heating sources than comparing FIR surface brightnesses directly to star-formation tracers, since brightness ratios normalize out the dust column density.

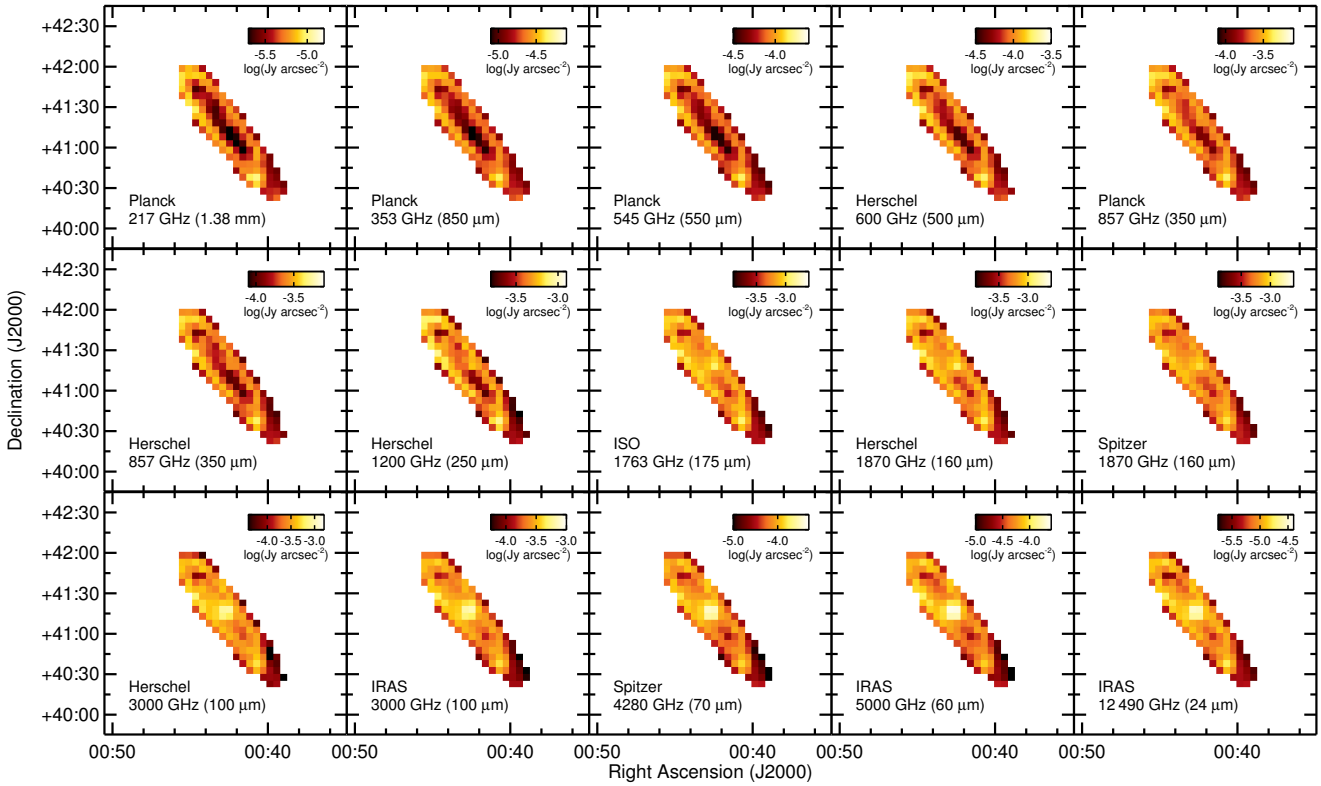

Fig. 5. Masked and pixelized 5′ data set ordered in increasing frequency (decreasing wavelength). The maps are $3^\circ \times 3^\circ$ in size. There is a clear change of morphology as frequency increases, with the rings being most prominent at the lower frequencies, and the nucleus being highlighted at higher frequencies.

We studied the dust heating sources in M 31 using surface brightness ratios measured in all *Planck* data at frequencies of 217 GHz and above (1.38 mm and shorter wavelengths), as well as in *Herschel*, ISO, *Spitzer*, and IRAS data. We convolved all of the high-resolution data (marked with "H" in Table 1) to 5′ resolution using a Gaussian kernel. We then rebinned the data to 5′ pixels; we selected this size because it is the same size as the beam, and so the signal in each pixel should be largely independent of the others. It is important to do this repixelization in order to avoid the appearance of artificial correlations in the data. We masked out data from outside the optical disc of the galaxy by requiring the pixel centre to be less than 22 kpc away from the centre of M 31 (which is equivalent to a 1°.42 radius along the major axis). To avoid pixels strongly affected by foreground or background noise, we only used data from pixels that had been detected in the 353 GHz (850 μm) image at 10 times the rms uncertainty in the data (measured in a 10×10 pixel region of sky to the far bottom-left of the data set used here). We also removed pixels at the top-left corner of the images, where the data have been contaminated by bright cirrus structures in the foreground. Finally, we removed pixels at the edge of the optical disc, which primarily sample a combination of background emission and emission from the wings of the beams for sources in the dust ring. This leaves 126 independent data points. We look at colour ratios in adjacent bands of the same telescope to minimize the effect of different telescope beams on the results; the exception to this is the highest frequency comparison, where we have no alternative but to compare *Spitzer* with *Herschel* data.

The rebinned data are shown in Fig. 5. The 10 kpc ring is present at all frequencies, but emission from the centre of the galaxy becomes more prominent as the frequency increases. At 1800 GHz (170 μm), both sources are approximately similar in surface brightness. The bright feature at the southern end of M 31 (source "S6" in Fig. 3) is clearly present at all frequencies, although it is more notable at $\nu < 1700$ GHz. There is a change of morphology apparent as frequency increases, with the rings being most prominent at the lower frequencies, and the nucleus being highlighted at higher frequencies.

Figure 6 shows the surface brightness ratios between adjacent frequency bands in the combined *Planck* and ancillary data set, where e.g., S_{545}/S_{353} denotes the colour ratio between 545 and 353 GHz (0.55 and 0.85 mm). The ratios of lower frequency bands (i.e., the *Planck* bands) appear to smoothly decrease with radius, although the data are somewhat noisy at S_{545}/S_{353}. The 10 kpc ring is hardly noticable at all in the lower frequency ratio maps. In the higher frequency ratio maps (e.g., the S_{4280}/S_{3000} map), the ring is much more prominent, and the colours also appear enhanced in a compact region around the nucleus.

These results imply that the different frequencies are detecting dust heated by different sources. At higher frequencies, the enhanced surface brightness ratios in the ring and the nucleus indicate that the dust is being heated by the star-forming regions in these structures. At lower frequencies, however, the ratios vary more smoothly with radius, and the ring does not appear to be as enhanced as in the data for the higher frequencies. This is consistent with dust heating being dominated by the total stellar population, including stars in the bulge of the galaxy, which should vary smoothly with radius (as has been suggested for other galaxies by Bendo et al. 2010, 2012a).

5.2. Determination of dust heating mechanism

To link the surface brightness ratios to heating sources, we compared the ratios to tracers of the total stellar population and star

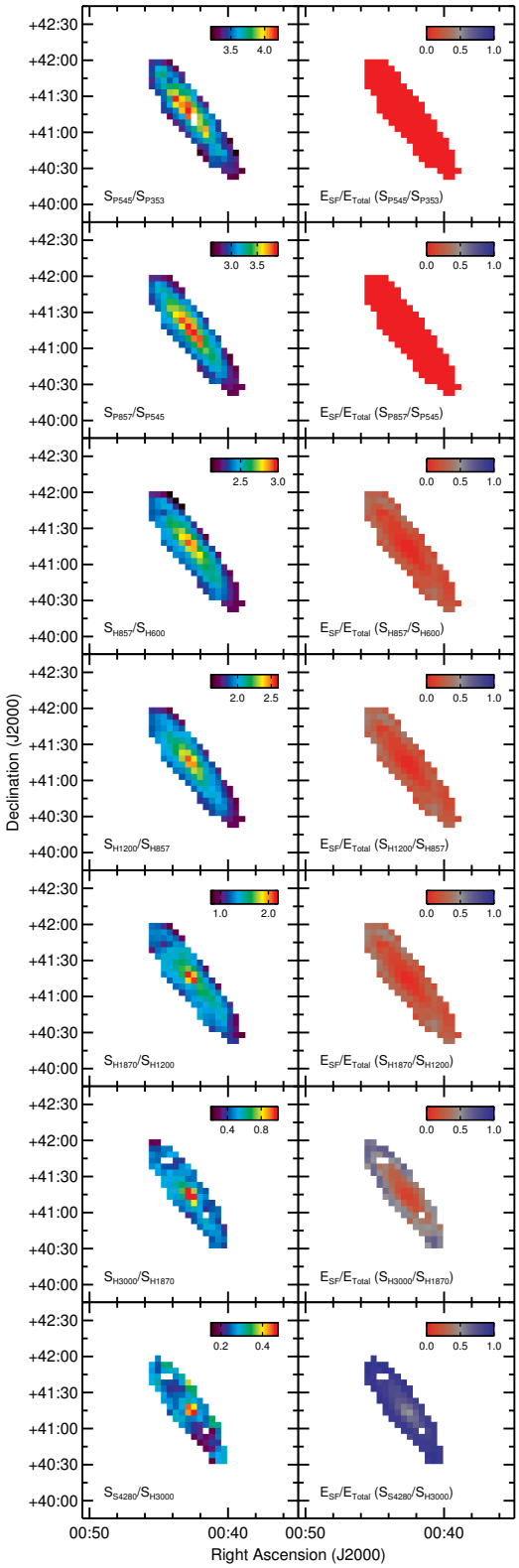

Fig. 6. *Left*: colour ratio plots with 5′ pixels. The 5′ pixels are slightly bigger than the beam size, such that the signal they contain is largely independent. The colour ratios for the lower frequency plots do not trace the local features; rather, they depend on the galactocentric distance. The higher frequency plots – in particular the highest frequency one – trace the local structure much more. *Right*: images of the relative contribution of star formation to heating the dust traced by the specified pair of frequencies. These maps were derived using Eq. (2) and the parameters in Table 2. *Top to bottom*: $S_{\rm P545}/S_{\rm P353}$, $S_{\rm P857}/S_{\rm P545}$, $S_{\rm H857}/S_{\rm H600}$, $S_{\rm H1200}/S_{\rm H857}$, $S_{\rm H1874}/S_{\rm H1200}$, $S_{\rm H3000}/S_{\rm H1874}$, and $S_{\rm S4280}/S_{\rm H3000}$.

formation. As a tracer of the total stellar population, we used the *Spitzer* 3.6 μm image, which is generally expected to be dominated by the Rayleigh-Jeans tail of the photospheric emission from the total stellar population (Lu et al. 2003). While the 3.6 μm band may also include roughly 1000 K dust emission from star-forming regions (Mentuch et al. 2009, 2010), this effect is usually only a major issue in late-type galaxies with relatively strong star formation compared to the total stellar surface density. A high infrared-to-visible ratio or a dominant active galactic nuclei (AGN) could also contaminate the 3.6 μm emission; however, neither of these issues are present in M 31. We used the *Spitzer* 24 μm image as a star-formation tracer, as this has been shown to generally originate from SFR dust (Calzetti et al. 2005, 2007; Prescott et al. 2007; Zhu et al. 2008; Kennicutt et al. 2009), although we caution that it is possible for some 24 μm emission to originate from dust heated by the diffuse interstellar radiation field from older stars (e.g., Li & Draine 2001; Kennicutt et al. 2009). The 24 μm band also includes a small amount of stellar emission; this was removed by multiplying the 3.6 μm image by 0.032 and then subtracting it from the 24 μm image, as described by Helou et al. (2004). While we could use 24 μm data combined with Hα or ultraviolet emission to trace both obscured and unobscured star formation (as suggested by, e.g., Leroy et al. 2008 and Kennicutt et al. 2009), the publicly-available data have problems that make them difficult to include in our analysis[6]. Bendo et al. (2015) have demonstrated that using the 24 μm data as a star-formation tracer for this analysis will yield results that are similar to using a composite Hα and 24 μm star-formation tracer (to within about 5%), so given the issues with the ultraviolet and Hα we will use solely 24 μm emission as our nominal star-formation tracer. We also use the combination of the 24 μm and far-ultraviolet (FUV) data, using the foreground star-subtracted GALEX data from Ford et al. (2013) and Viaene et al. (2014), to check whether this has a significant impact on our results. We return to the results of using this star-formation tracer later in this section.

In Fig. 7, we show the surface brightness ratios for the binned data as a function of the 3.6 and 24 μm data. Statistics on the relations are given in Table 2. Only the S_{4280}/S_{3000} ratio shows a stronger correlation with the 24 μm emission than the 3.6 μm emission, which implies that only the dust dominating emission at ≥4280 GHz (≤70 μm) is heated by star-forming regions. All the other ratios are more strongly correlated with 3.6 μm emission, which demonstrates that the total stellar populations, and not solely the star forming regions, are heating the dust observed below 3000 GHz (100 μm).

As an additional assessment of the heating sources of the dust observed at these frequencies, we fit the S_{545}/S_{353}, S_{857}/S_{545}, S_{1200}/S_{857}, $S_{1874/1200}$, $S_{3000/1870}$, and S_{4280}/S_{3000} ratio data to the 3.6 and 24 μm data using the equation

$$\ln\left(\frac{S_{\nu_1}}{S_{\nu_2}}\right) = \alpha \ln(I_{\rm SFR} + A_1 I_{\rm stars}) + A_2. \quad (1)$$

This equation, derived from the Stefan-Boltzmann law by Bendo et al. (2012a), relates the surface brightness ratios of the dust with the dust heating sources. The ratio S_{ν_1}/S_{ν_2} on the left side

[6] The publicly-available Hα data, such as from the Virginia Tech Spectral-Line Survey, Dennison et al. (1998), contain artefacts from incompletely-subtracted foreground stars, as well as incompletely-subtracted continuum emission from the bulge of M 31, and are therefore unsuitable for our analysis. The publicly-available ultraviolet data contain multiple bright foreground stars, as well as emission from older stellar populations within M 31.

Table 2. Results from fitting Eq. (1) to the colour ratio data, including the covariance terms between the fitted parameters.

Ratio	α	A_1	A_2	E_{SF}/E_{Total}	Cov(α, A_1)	Cov(α, A_2)	Cov(A_1, A_2)	C(3.6)	C(24)
S_{P545}/S_{P353}	0.071 ± 0.01	...	1.25 ± 0.01	0	...	-4.7×10^{-5}	...	0.85	0.51
S_{P857}/S_{P545}	0.103 ± 0.018	...	1.10 ± 0.01	<0.13	...	-9.3×10^{-5}	...	0.86	0.71
S_{H857}/S_{H600}	0.085 ± 0.009	2.40	0.77 ± 0.04	0.19 ± 0.12	−0.0069	5.7×10^{-5}	−0.096	0.88	0.57
S_{H1200}/S_{H857}	0.108 ± 0.008	2.04	0.54 ± 0.04	0.22 ± 0.09	−0.0048	8.3×10^{-5}	−0.058	0.90	0.61
S_{H1874}/S_{H1200}	0.180 ± 0.013	1.82	0.06 ± 0.05	0.23 ± 0.08	−0.0063	0.00022	−0.047	0.85	0.61
S_{H3000}/S_{H1870}	0.30 ± 0.03	0.69	−0.95 ± 0.04	0.44 ± 0.07	−0.0039	0.00036	−0.0076	0.66	0.62
S_{S4280}/S_{H3000}	0.37 ± 0.04	0.077	−1.35 ± 0.02	0.85 ± 0.04	−0.00049	0.00015	−0.00052	0.34	0.65
S_{P545}/S_{P353}	0.063 ± 0.014	...	1.27 ± 0.01	0	...	-5.0×10^{-5}	...	0.85	0.52
S_{P857}/S_{P545}	0.102 ± 0.018	...	1.10 ± 0.01	<0.15	...	-9.3×10^{-5}	...	0.86	0.71
S_{H857}/S_{H600}	0.095 ± 0.009	2.40	0.77 ± 0.04	0.19 ± 0.12	−0.0075	6.1×10^{-5}	−0.093	0.88	0.57
S_{H1200}/S_{H857}	0.108 ± 0.008	2.04	0.54 ± 0.04	0.22 ± 0.09	−0.0048	8.3×10^{-5}	−0.058	0.90	0.61
S_{H1874}/S_{H1200}	0.180 ± 0.013	1.82	0.06 ± 0.05	0.23 ± 0.08	−0.0063	0.00022	−0.047	0.85	0.61
S_{H3000}/S_{H1870}	0.30 ± 0.03	0.69	−0.95 ± 0.04	0.44 ± 0.07	−0.0039	0.00036	−0.0076	0.66	0.62
S_{S4280}/S_{H3000}	0.37 ± 0.04	0.077	−1.35 ± 0.02	0.85 ± 0.04	−0.00049	0.00015	−0.00052	0.34	0.65
S_{P545}/S_{P353}	0.071 ± 0.014	...	−0.28 ± 0.18	0	...	-4.9×10^{-5}	...	0.85	0.38
S_{P857}/S_{P545}	0.101 ± 0.017	...	0.36 ± 0.69	<0.13	...	0.00421	...	0.86	0.60
S_{H857}/S_{H600}	0.085 ± 0.009	1.71	0.80 ± 0.05	0.16 ± 0.11	−0.0056	1.4×10^{-4}	−0.074	0.88	0.46
S_{H1200}/S_{H857}	0.109 ± 0.009	1.27	0.59 ± 0.05	0.21 ± 0.09	−0.0048	1.8×10^{-4}	−0.054	0.90	0.50
S_{H1874}/S_{H1200}	0.183 ± 0.014	1.05	0.16 ± 0.05	0.24 ± 0.08	−0.0047	0.00041	−0.027	0.85	0.51
S_{H3000}/S_{H1870}	0.31 ± 0.03	0.38	−0.77 ± 0.05	0.44 ± 0.06	−0.0021	0.00076	−0.0049	0.66	0.56
S_{S4280}/S_{H3000}	0.39 ± 0.05	0.055	−1.34 ± 0.04	0.81 ± 0.04	−0.00030	0.00013	−0.00046	0.34	0.41

Notes. Upper limits are 1σ. The last two columns are the correlation coefficients (C) from Fig. 7. *Top*: using `SMICA` CMB subtraction. *Middle*: using `NILC` CMB subtraction. *Bottom*: using the combination of 24 μm and FUV emission as the star-formation tracer, with `SMICA` CMB subtraction. *Planck* data are marked by "P," *Herschel* data by "H," and *Spitzer* data by "S."

of the equation is related to the dust temperature through a power law (assuming that the dust seen in any pair of frequencies has only one temperature or a narrow range of temperatures). Therefore, S_{ν_1}/S_{ν_2} can ultimately be expressed as a function of the total energy emitted by the dust using a version of the Stefan-Boltzmann law modified for dust with an emissivity function that varies as ν^{β}. The I_{SFR} and I_{stars} terms represent the energy absorbed by the SFR dust (traced by the 24 μm band) and the ISRF dust (traced by the 3.6 μm band). The slope α and the scaling terms A_1 and A_2 are free parameters in the fit. The scaling terms will adjust the I_{SFR} and I_{stars} data to account for the fraction of light from those sources that is absorbed by the dust.

After Eq. (1) has been fit to the data, the relative magnitudes of the I_{SFR} and $A_1 I_{stars}$ terms can be used to estimate the fraction of dust heating (traced by the variation in the surface brightness ratios for any pair of frequencies) that can be related to each heating source. We calculated the fraction of dust heating from star-forming regions using

$$\frac{E_{SF}}{E_{Total}} = \frac{I_{SFR}}{I_{SFR} + A_1 I_{stars}}. \quad (2)$$

The resulting parameters from fitting Eq. (1) to the data are given in Table 2. We also give the resulting E_{SF}/E_{Total} values based on the flux density measurements integrated over the disc of the galaxy. Uncertainties in the α, A_2, and E_{SF}/E_{Total} values are estimated using a Monte Carlo approach, but we did not report uncertainties for the A_1 term because the A_1 and A_2 terms become degenerate when $I_{SFR} \ll A_1 I_{stars}$ and because the A_1 term is poorly constrained where $I_{SFR} \gg A_1 I_{stars}$, resulting in high uncertainties for the scaling terms. Figure 6 shows the E_{SF}/E_{Total} maps calculated using Eq. (2) and the best fitting A_1 terms. What all of these data demonstrate is that the relative fraction of SFR dust decreases when going from higher frequencies to lower frequencies. The results for the S_{4280}/S_{3000} ratio show that around 90% of the colour variations can be related to SFR dust. In the centre of the galaxy, however, more than 50% of the emission at these frequencies originates from dust heated by the total stellar population, including stars in the bulge. The S_{857}/S_{545} and S_{545}/S_{353} colours show that the dust emission at these frequencies primarily originates from ISRF dust. The contribution of SFR dust, even in the ring, is relatively weak. In fact, when Eq. (1) was fit to the S_{545}/S_{353} data, the resulting parameters indicated that the contribution from the I_{SFR} component was negligible; the terms in Table 2 were adjusted to normalize A_1 to 1. The transition between SFR dust and ISRF dust is at around 3000 GHz.

We have also carried out this analysis using data where the `NILC` map was used to subtract the CMB. We find that the results are not very sensitive to the contamination of the CMB map by M 31. The results from fitting Eq. (1) to the `NILC`-subtracted data are shown in the middle section of Table 2 and are well within the stated uncertainties. The apparently different values for A_1 and A_2 for the S_{857}/S_{545} ratios are due to the degeneracy in these parameters, as described above.

We have also run this analysis using the combination of 24 μm and far-ultraviolet data to trace both the obscured and unobscured star formation. We combine the two datasets to obtain the equivalent corrected 24 μm emission (for ease of comparison with the results given above) using

$$I_{SFR} = (I_{24} - 0.032\, I_{3.6}) + 25.3\left(I_{FUV} - 8.0\times10^{-4}\, I_{3.6}\right), \quad (3)$$

where the corrections for the old stellar population emission are as per Ford et al. (2013), and the rescaling of the FUV emission uses the combination of the 24 μm and FUV coefficients given in the calculation of the combined star formation rate in Leroy et al. (2008). The results from this are given in the bottom section of Table 2. The addition of FUV data to the star-formation tracer

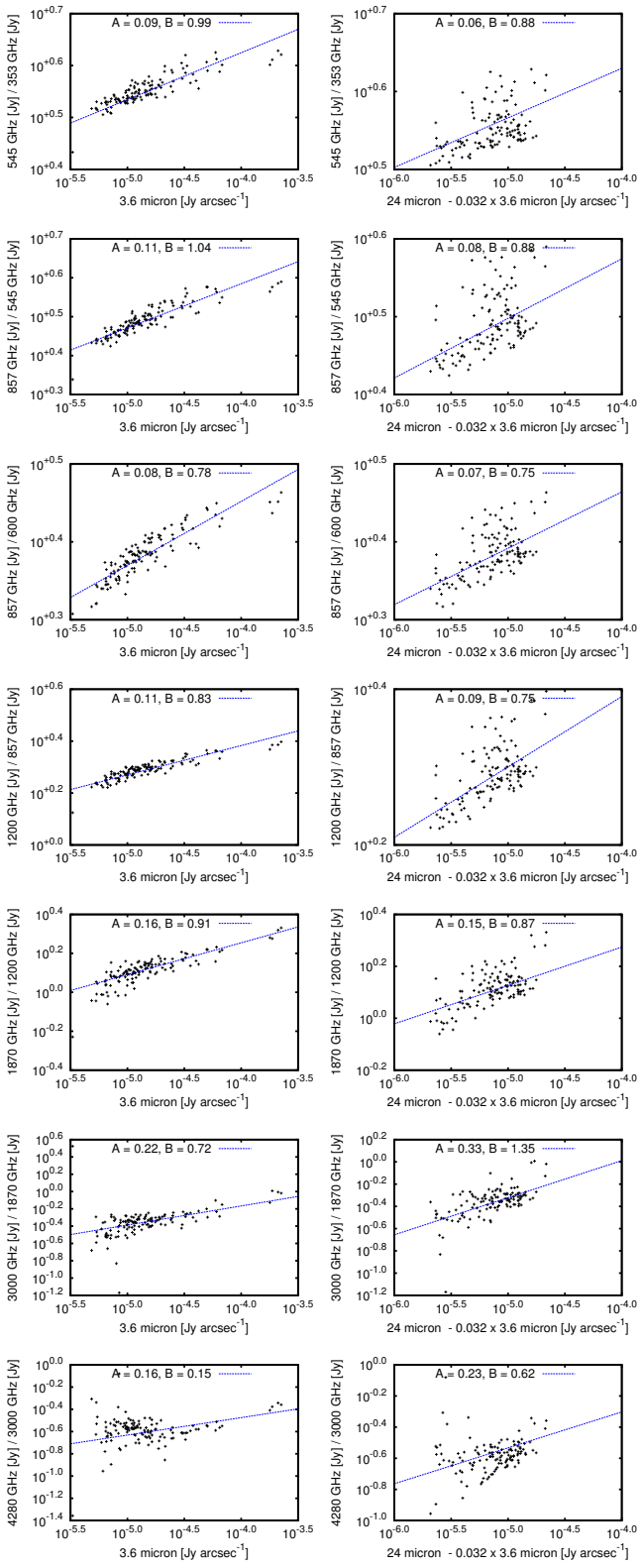

Fig. 7. Correlations between colour ratios and 3.6 μm, tracing the stellar population (*left*), and 24 μm, tracing star formation regions (*right*). The best fits of the form $\log_{10}(y) = A \log_{10}(x) + B$ are shown by the solid lines. The correlation with 3.6 μm emission becomes less significant as the frequencies of the colour ratios increase, whilst the 24 μm correlation becomes more significant. The correlation values are given in Table 2.

changes our results by less than 5%, which is a similar level to the effect that Bendo et al. (2015) found when switching between uncorrected Hα, combined Hα and 24 μm emission, and 24 μm emission by itself as star-formation tracers.

Groves et al. (2012) and Smith et al. (2012) have also examined dust heating in M 31 using *Herschel* data that overlaps with the *Planck* frequencies. Both groups found that the dust emission in the centre of M 31 appears to be heated by the total stellar population, including the bulge stars, which agrees with our results. However, Smith et al. (2012) found that the dust temperatures in the ring may be weakly correlated with star formation activity and is not correlated with the total stellar emission, whereas we find that about 50% of the dust in the ring seen below 3000 GHz is still heated by the total stellar population. This is probably related to the different analyses and underlying assumptions used. Smith et al. (2012) assume that a single modified blackbody spectrum can accurately describe all data between 600 and 1870 GHz (500 and 160 μm), whereas we treated each pair of frequency bands independently and found that the 545–1870 GHz (550–160 μm) range contains dust from two different thermal components heated by different sources. Hence, the Smith et al. (2012) fits may have been unduly influenced by relatively small amounts of hot dust that may have masked the presence of the colder dust within the ring and therefore may not have been able to detect the dust primarily emitting at <870 GHz (>350 μm) that is heated by the diffuse interstellar radiation field.

The conclusion that the dust in M 31 seen at *Planck* frequencies is primarily heated by the total stellar population and not just the star forming regions is broadly consistent with the recent *Herschel* results using similar techniques (Bendo et al. 2010, 2012a; Boquien et al. 2011), as well as some of the older IRAS studies of dust heating in our Galaxy and other nearby galaxies (e.g., Lonsdale Persson & Helou 1987; Walterbos & Schwering 1987; Sauvage & Thuan 1992; Walterbos & Greenawalt 1996). Some dust emission and radiative transfer models for galaxies (e.g., Draine et al. 2007; Popescu et al. 2011) include two dust components: diffuse dust heated by a general interstellar radiation field; and dust heated locally by star forming regions. The results here are broadly consistent with the characterisation of the dust emission by these models. However, we observe the transition between SFR dust and ISRF dust at 70–100 μm, whereas in the model fits shown by Draine et al. (2007), the transition generally takes place at shorter wavelengths (below 70 μm), while De Looze et al. (2014) finds the transition to be around 60 μm, and the model of Natale et al. (2015) has the transition at around 30 μm. These results are, of course, dependent on the implementation details of the modelling of the two components.

6. SEDs at 5′ resolution

We now move on to investigate and quantify the distribution of dust temperatures and spectral indices within M 31 by fitting thermal dust spectra to the 5′ data set (as described in the previous section) comprised of *Planck*, *Spitzer*, IRAS, and ISO data. We use the dust heating fraction that was quantified in the previous section in order to focus only on the colder dust that is heated by the total stellar population.

To remove the effect of the background, including offsets in the map, the average contribution from the CIB, and the average Galactic cirrus contribution, we background-subtract the *Planck* and IRAS maps. To do this we use the mean flux density in two 13 × 13 pixel areas to the bottom-left and top-right of the 2D maps, which straddle the galaxy at locations that are well away from both the emission from M 31 and our Galaxy

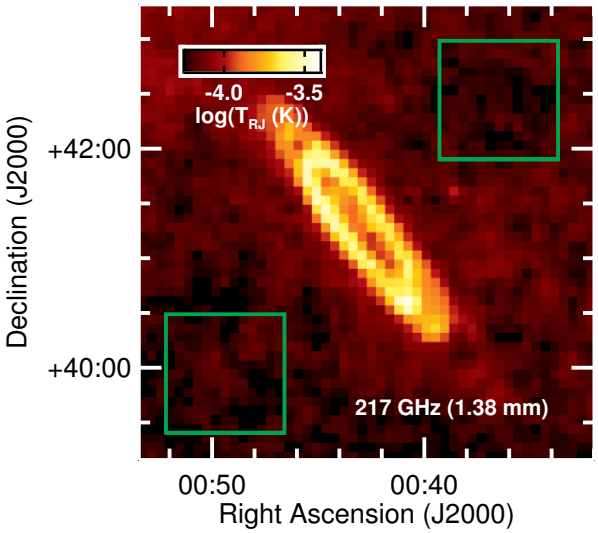

Fig. 8. *Planck* 217 GHz map at 5′ resolution showing the two regions used to calculate the background and rms (top-right and bottom-left).

(see Fig. 8). We also use the rms scatter within these regions to estimate the uncertainty in the data caused by noise and cirrus contamination. As the *Spitzer* and ISO data have already been background-subtracted, and as the maps do not extend to the background subtraction regions that we are using for the other data, we do not background-subtract these further. We assess the uncertainty on each pixel by combining the calibration uncertainties (as per Table 1) in quadrature with the rms of the map estimated in the same regions as the background subtraction or, for the *Spitzer* data, the rms of the data outside the mask. We have estimated the background and rms using different regions and found consistent results. These uncertainties also take into account the contribution of the cirrus and CIB structure on smaller scales; as the rms is in the range 0.015–0.37 Jy (depending on the frequency), this is generally small compared to the signal from M 31, except in the outermost rings.

6.1. Fitting method

We focus on fitting the SEDs of the ISRF dust rather than the total SED. The ISRF dust will be the most massive component of the interstellar dust, as it is the coldest dust component in the galaxy and also the most dominant source at ≤3000 GHz (≥100 μm, see e.g., Draine et al. 2007).

We use the maps of the ratio of the contribution of star formation and the old stellar population shown in Fig. 6 to rescale the flux densities of the 545, 857, 1200, 1874, 3000, and 4280 GHz (550, 350, 250, 160, 100, and 70 μm) data points. We use the *Planck* 353 GHz (850 μm) and *Herschel* 600 GHz (500 μm) maps as zero points and rescale the higher frequency flux densities based on the ratio maps (e.g., the 857 GHz/350 μm map is rescaled by $[1 - R_{545}^{857}]$) where $R = E_{\rm SF}/E_{\rm Total}$ between the indicated frequencies within the pixel; we refer to these values as "rescaled flux densities" in the following analysis. At the lowest frequencies, nearly all of the dust emission is attributed to the global stellar population component, while at higher frequencies the ratio will indicate how much energy in the higher frequency band originates from SFR dust relative to the lower frequency band. If the relative fraction of SFR dust is very low, then the ratios can be used as an approximate way to rescale the flux densities for the higher frequency bands. We also fit the global SED to demonstrate the difference that the rescaling makes on the measured dust properties.

We carry out a least-squares fit using a single modified blackbody function with a normalization based on the 353 GHz (850 μm) optical depth, i.e.

$$S_{\rm dust}(\nu) = 2\,h\,\frac{\nu^3}{c^2}\,\frac{1}{e^{h\nu/kT_{\rm dust}} - 1}\,\tau_{353}\left(\frac{\nu}{353\,{\rm GHz}}\right)^{\beta_{\rm dust}}\Omega. \quad (4)$$

Independent fits within each 5′ pixel (with solid angle Ω) are used to derive the optical depth at 353 GHz (850 μm), τ_{353}, and the dust temperature $T_{\rm dust}$. We use $T_{\rm dust}$ = 15 K as the starting value for the fit. We fix the dust spectral index at $\beta_{\rm dust}$ = 2.0, as used by Li & Draine (2001; see discussion in the next paragraph); we also look at the consequences of allowing this to vary in Sect. 6.3. We exclude the *Planck* 217 GHz (1.38 mm) data from the fit because of CO contamination, and we do not use data above 3000 GHz (100 μm), because we are only considering the large dust grain population rather than small dust grains or PAH emission. We also exclude data where we have *Planck* or *Herschel* data at the same frequency. In practice, this means that we fit to the *Planck* 353, 545, and 857 GHz (850, 550, and 350 μm) bands, and the *Herschel* 600, 1200, 1874, and 3000 GHz (500, 250, 160, and 100 μm) bands. We use the other data sets for comparison only. During the fitting process we iteratively colour correct the data based on the model.

We also calculate the dust mass per arcminute based on τ_{353} (chosen to reduce the sensitivity of the calculation to the dust temperature) via

$$M_{\rm dust} = \frac{\tau_{353}\Omega D^2}{\kappa_{353}} \quad (5)$$

(Hildebrand 1983), where we use the dust mass absorption coefficient at 353 GHz (850 μm), κ_{353} = 0.0431 m^2 kg^{-1}, as being representative of the diffuse interstellar medium (Li & Draine 2001; this value agrees well with that measured by Planck Collaboration Int. XVII 2014; and is also close to the value measured in Planck Collaboration XI 2014). The value of κ_{353} depends on $\beta_{\rm dust}$ (see Planck Collaboration Int. XVII 2014); however the value of κ_{353} that we use here is from a specific model and should not be rescaled. As such we only use Eq. (5) to calculate the dust masses for fits where we have fixed $\beta_{\rm dust}$ = 2.0, which is approximately the spectral index for the carbon dust in the model of Li & Draine (2001). When we allow $\beta_{\rm dust}$ to vary we show the amplitudes of the best-fitting functions (τ_{353}). For the fits where $\beta_{\rm dust}$ = 2.0, the dust mass per pixel can be converted into optical depth by dividing by $1.45 \times 10^{10}\,M_\odot$. We quote dust mass surface densities in units of $M_\odot$ kpc^{-2}; along the major axis of M 31 there is 228 pc per arcmin, which after adjusting for inclination gives 0.273 kpc^2 per arcmin^2.

6.2. Representative SEDs

We show representative SEDs of individual pixels in Fig. 9, looking at the nuclear region, positions on the north and south sides of the 10 kpc ring, and pixels containing the outer spiral arm structure to the south of the galaxy. These plots include both SED fits to the entire spectrum, and to the emission that is related to heating by the stellar population (with both original and rescaled flux densities shown in the SED).

We find that the long wavelength data are generally well-fitted by a single modified blackbody with a fixed spectral index of 2.0, with χ^2 values between 0.9 and 20.7 and an average value of $\bar{\chi}^2$ = 7.6 ($N_{\rm d.o.f.}$ = 5). In general we find a similar χ^2 for

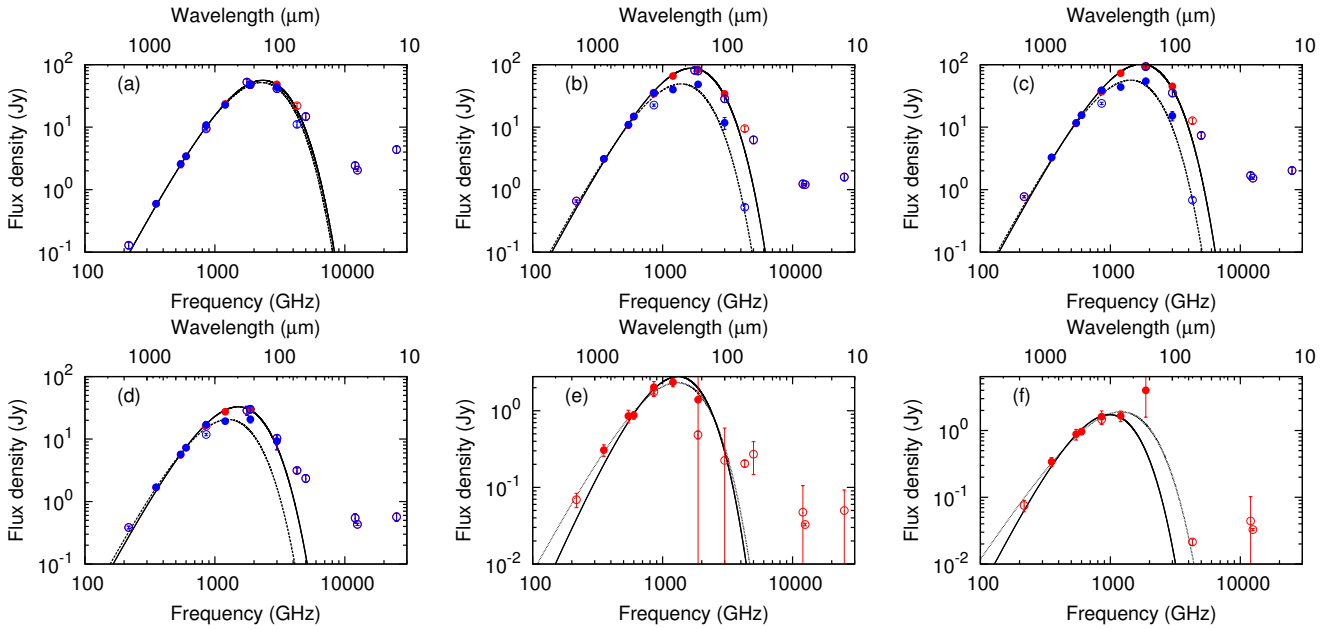

Fig. 9. Representative SEDs in various parts of M 31. The solid line shows the fit of the modified blackbody with $\beta = 2$ to the full flux densities (shown in red), and the dashed line shows the fit to the rescaled flux densities (shown in blue). Only the filled data points are used in the fits. The fit parameters are discussed in the text. *Top row*: **a)** the SED of a pixel in the nuclear region ($00^h42^m30^s$, $+41°09'$); **b)** the northern edge of the 10 kpc ring ($00^h45^m40^s$, $+41°54'$); **c)** the bright pixel in the southern end of M 31 ($00^h40^m45^s$, $+40°39'$). *Bottom row*, outer spiral arms: **d)** 14.8 kpc arm ($00^h39^m53^s$, $+40°23'$); **e)** 22 kpc arm ($00^h37^m43^s$, $+39°58'$); and **f)** 26 kpc arm ($00^h36^m52^s$, $+39°43'$). The last two SEDs also show a variable $\beta_{\rm dust}$ fit with a dotted line.

the rescaled SEDs compared to the original SEDs. These values of χ^2 indicate that the estimates of the uncertainties in the data are conservative; however, the data points are not independent, as the maps are correlated due to their common calibration schemes, an estimate of which has been incorporated in these uncertainties (see Sects. 2 and 3).

In the nuclear region, the data fit the model well (see the left-hand panel of Fig. 9), and there is a clear separation between the large grain contribution compared with the small grains, since the large grain contribution peaks at around 55 Jy at approximately 140 μm (2 THz) compared with only 2 Jy at 25 μm (12 THz). This pixel is dominated by ISRF dust up to high frequencies (as also seen by Viaene et al. 2014), such that there is not a large difference between the original and rescaled SED fits. The model residual at 217 GHz (1.38 mm), which could be ascribed to CO emission, has the same amplitude as the uncertainty on the data point. For the original SED, we find a mass surface density of $(0.95 \pm 0.05) \times 10^4\,M_\odot\,{\rm kpc}^{-2}$ and a temperature of (22.7 ± 0.3) K with $\chi^2 = 1.31$ ($N_{\rm d.o.f.} = 5$). We find very similar results for the rescaled SED; we find a mass surface density of $(1.03 \pm 0.06) \times 10^4\,M_\odot\,{\rm kpc}^{-2}$ and a temperature of (21.9 ± 0.3) K, with $\chi^2 = 1.25$ ($N_{\rm d.o.f.} = 5$). This temperature agrees well with that of Fritz et al. (2012), who found (22.2 ± 0.4) K from *Herschel* data. However, it is considerably less than the approximately 35 K in the 14″ study by Groves et al. (2012), which is due to: the lower resolution used here; that the core of M 31 is spread out across four pixels in this analysis; and the steep temperature gradient in the core of M 31. The nuclear region is the warmest in the entire galaxy, which is unsurprising, since warmer dust is present in spiral galaxies with large bulges (Sauvage & Thuan 1992; Engelbracht et al. 2010).

Moving to the 10 kpc ring, we find that this has higher optical depth/dust masses than the rest of M 31, but that the dust heated by the global stellar population has lower temperatures than the dust heated by the global stellar population in the nucleus. However, there are multiple heating processes present, as demonstrated by the rescaled SEDs being much lower than the unscaled SEDs, and the SFR dust will be warmer than the dust emission studied here. We present an example on the northern edge of the ring in the top-centre panel of Fig. 9. In this pixel, the rescaled (original) SEDs are fitted by a mass surface density of $(8.0 \pm 0.3) \times 10^4\,M_\odot\,{\rm kpc}^{-2}$ [$(8.9 \pm 0.4) \times 10^4\,M_\odot\,{\rm kpc}^{-2}$], and a temperature of (16.2 ± 0.08) K [(15.5 ± 0.2) K], with χ^2 of 10.4 [9.8] ($N_{\rm d.o.f.} = 5$). As with the nucleus, the large dust grain component is significantly brighter than the small dust grain emission. The residual at 217 GHz (1.38 mm) is (0.08 ± 0.03) Jy, implying that there is some CO emission in this pixel. We also look at a pixel on the southern edge, which is particularly bright at low frequencies, shown in the right-hand panel of Fig. 9. Once more, there is a good separation between the lower-frequency large dust grain and the higher-frequency small dust grain populations. The temperature and spectral indices are similar to the northern pixel, with the rescaled (original) SEDs fitted by a mass surface density of $(8.3 \pm 0.3) \times 10^4\,M_\odot\,{\rm kpc}^{-2}$ [$(9.2 \pm 0.4) \times 10^4\,M_\odot\,{\rm kpc}^{-2}$] and a temperature of (16.7 ± 0.1) K [(15.7 ± 0.1) K], and χ^2 of 13.6 [9.6] ($N_{\rm d.o.f.} = 5$). The residual at 217 GHz (1.38 mm) in this pixel is (0.16 ± 0.03) Jy [(0.14 ± 0.03) Jy], implying that there is some CO emission detected by *Planck* in this (and neighbouring) pixels. This is 22% [18%] of the total emission at 217 GHz (1.38 mm) in that pixel.

We also look at the dust properties in the outermost spiral arms of M 31. *Herschel* observations of M 31 (Fritz et al. 2012) find dust distributed in three ring-shaped structures extending out to 21, 26, and 31 kpc, with dust temperatures of 19.2, 18.2, and 17.1 K (all with uncertainties of approximately ±0.2 K) respectively, derived using a single component $\beta_{\rm dust} = 2$ dust model. We look at three pixels on the 14.8, 22 and 26 kpc spiral arms, the SEDs for which are shown in the bottom row of Fig. 9. We do not include *Spitzer* or ISO data in the fits for the outermost two spiral arm SEDs. The background subtraction method used for the *Spitzer* data removed large-scale background structures in a way that was different than the background subtraction in

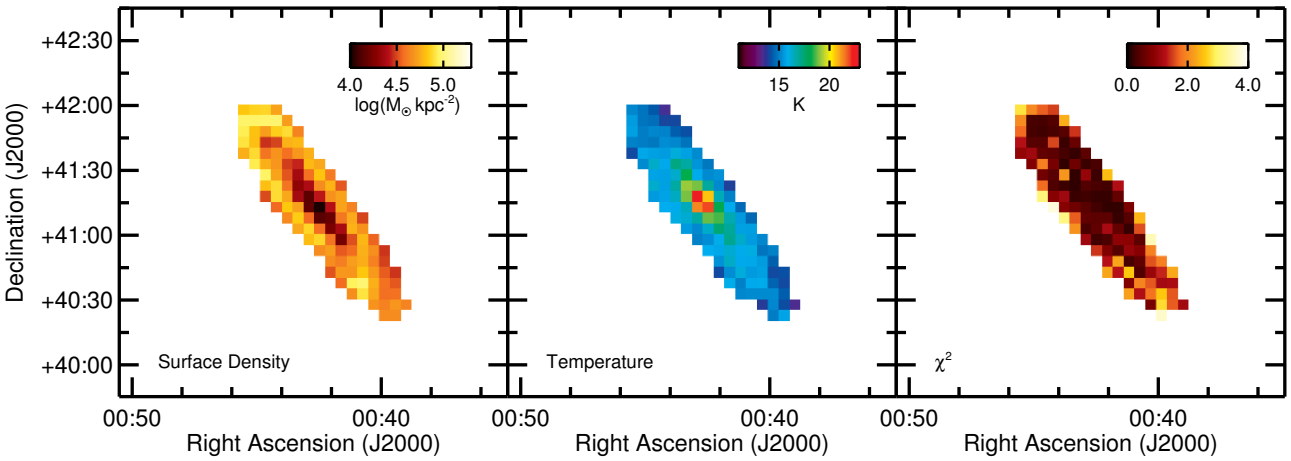

Fig. 10. Maps of the fitted dust mass surface density (*left*), temperature (*middle*) and reduced χ^2 (*right*) for a one-component fit to the 5′ data set using the rescaled SEDs. The ring morphology can be clearly seen in the dust mass density, while the dust temperature decreases with galactocentric distance.

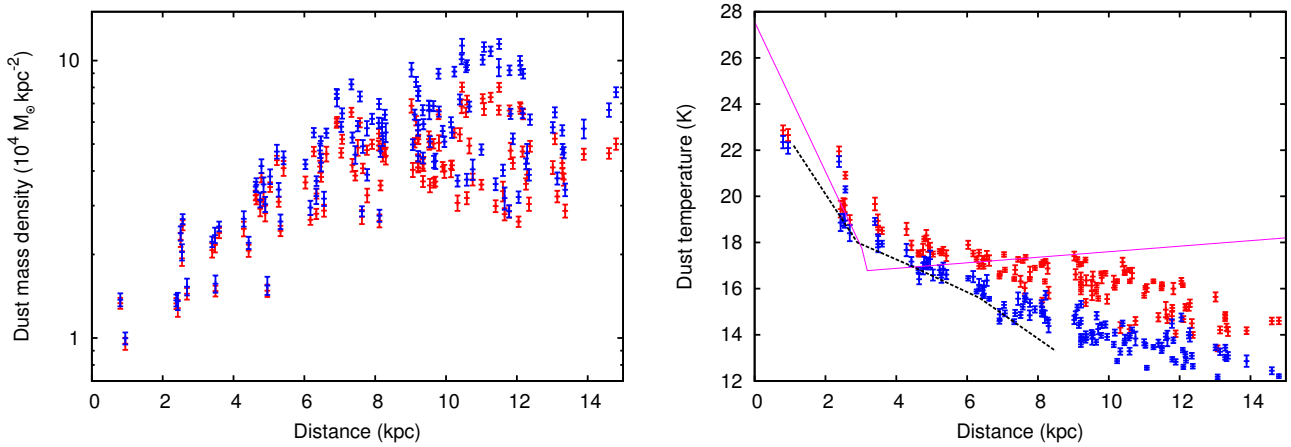

Fig. 11. The fitted dust mass surface density (*left*) and dust temperature (*right*) as a function of galactocentric distance. Red points are from fitting the entire SED, while blue points are fitting to the fraction of the flux density that can be attributed to the dust heated by the global stellar population. Temperatures from Fritz et al. (2012) and Smith et al. (2012) are shown by the dashed black line and the solid magenta line, respectively; these differ from the analysis here due to the different dust models used and whether the dust spectral index has been allowed to vary or not. There is a systematic shift towards lower dust temperatures and higher dust masses with the rescaled SEDs.

other maps, and ISO did not map out that far. In addition, the 22 and 26 kpc arms were not included in the colour ratio analysis, so we consider the original rather than rescaled SED for those arms. The temperatures for these, using the *Planck* and *Herschel* data and $\beta_{\rm dust} = 2.0$, are (14.8 ± 0.2) K ($\chi^2 = 11.8$, , $N_{\rm d.o.f.} = 5$) (rescaled, (15.6 ± 0.3) K, $\chi^2 = 24.9$, $N_{\rm d.o.f.} = 4$), (12.7 ± 0.4) K ($\chi^2 = 7.9$, $N_{\rm d.o.f.} = 4$) and (9.6 ± 0.2) K ($\chi^2 = 3.9$, $N_{\rm d.o.f.} = 4$). The SEDs are also poorly fitted with a fixed $\beta_{\rm dust} = 2.0$, so we also try a variable $\beta_{\rm dust}$ fit for the outermost arms. We find a much flatter spectral index for these, with the 22 kpc ring at (15.0 ± 1.0) K and $\beta_{\rm dust} = 1.2 \pm 0.3$ ($\chi^2 = 2.2$, $N_{\rm d.o.f.} = 3$), and the 26 kpc ring at (14.7 ± 0.4) K and $\beta_{\rm dust} = 1.0 \pm 0.3$ ($\chi^2 = 2.4$, $N_{\rm d.o.f.} = 3$), although these fits lie above the 217 GHz data point that is not fitted in the data. These results for $T_{\rm dust}$ and $\beta_{\rm dust}$ could be biased as there are only a few higher frequency data points that constrain the peak of the SED. The lower temperatures found here (compared with those by Fritz et al. 2012) are driven by the inclusion of *Planck* data in the analysis.

6.3. Maps of the dust parameters

In Fig. 10 we plot the best-fit parameter values for the dust heated by the old stellar population, as well as the reduced χ^2 values for all pixels, with the dust mass density deprojected so that the pixels are in units of $M_\odot$ kpc^{-2}. The fitted dust temperature traces the stellar population, with the dust decreasing in temperature with distance from the centre of M 31. The dust mass traces the 10 kpc ring structure, with the highest masses in the north part of the ring and in the bright region in the south part of the ring. We have compared our dust masses with those from Planck Collaboration Int. XXIX (2014); after correcting their map for the inclination of M 31 we find that their dust mass estimates are approximately 30% higher than ours, which is due to the different dust modelling technique used as well as the different zero levels in the maps.

Figure 11 shows the dust mass density and temperature per pixel as a function of galactocentric distance, for both the entire and rescaled SEDs. The fits to the rescaled SEDs have lower temperatures and higher dust masses than the fits to the full SEDs, and the difference increases in significance as the galactocentric distance increases. The dust mass clearly increases from the nucleus outwards, peaking at the position of the ring (around 10 kpc), before decreasing again. The dust that is heated by the evolved stellar population is hottest in the centre of M 31 at about 22 K, and the temperature decreases down to around 14 K at the distance of the ring. These trends are

broadly comparable to those found by Fritz et al. (2012), which are shown by the dashed black line in the plot, and have the opposite trend at larger distances than the results of Smith et al. (2012), shown by the solid magenta line. The dust temperature behaviour as a function of distance most likely differs between these analyses due to the different dust models used, in particular whether the dust spectral index is fixed or allowed to vary; this will be discussed later in this section.

The temperatures from the rescaled and unscaled SEDs agree well with each other in the centre of the galaxy, but diverge from each other beyond about 5 kpc. We expect the SFR to contribute more to dust heating at larger distances from the centre as the bulge stars peak in the centre of the galaxy and the SFR peaks in the ring. At the centre of the galaxy, the old stellar population in the bulge dominates the ISRF, and the dust seen at wavelengths as short as 70 μm is heated by the ISRF, which means that the rescaled vs. unscaled SEDs should be essentially the same. The rescaled and unscaled SEDs may converge outside of the 10 kpc ring, but we lack the sensitivity to accurately measure the SED at larger radii and therefore cannot see this reconvergence.

We also combine the values from all pixels and fit a fixed $\beta_{\rm dust}$ model to the overall SED from M 31. We find that this has an average temperature for the rescaled [original] SED of (16.96 ± 0.13) K [(16.89 ± 0.12) K] and a combined dust mass of $(6.6 \pm 0.3) \times 10^7\,M_\odot$ [$(7.0 \pm 0.3) \times 10^7\,M_\odot$]. The combined dust mass from the fits to the individual pixels is $(3.6 \pm 0.3) \times 10^7\,M_\odot$ [$(4.1 \pm 0.3) \times 10^7\,M_\odot$], around a factor of two lower. This is the opposite of the results of Galliano et al. (2011), who found 50% higher dust masses when fitting data for the LMC at higher resolution compared to the integrated SED, and Aniano et al. (2012) who find up to 20% higher dust masses from fitting the resolved data for NGC 628 and NGC 6946. However it is in agreement with Smith et al. (2012) who, like us, find a significantly higher dust mass from the integrated SED than the individual pixel SEDs in M 31, and also Viaene et al. (2014) who find a dust mass 7% higher using an integrated SED. The difference between the masses is caused by different analyses using varying data sets and assumptions, as well as different weightings resulting from the morphology and temperature distribution within M 31. In the case of the LMC and other dwarf galaxies, warm dust in star forming regions are embedded within a dust component of cool large grains heated by a relatively weak diffuse interstellar radiation field. When integrating over large areas, the resulting temperatures are warmer and dust surface densities are lower than what would be found within individual subregions. In M 31 and other galaxies with large bulges (e.g., M 81; Bendo et al. 2010, 2012a), the temperature of large dust grains heated by the diffuse interstellar radiation field in the centres of the galaxies may be higher than the temperature of the large dust grains heated locally by star-forming regions in the outer disc. When integrating over an area that includes both the centre of the galaxy and the star forming ring, the inferred dust temperatures may appear lower and the dust surface densities may appear higher than what would be found in individual subregions within the galaxies. The combined dust mass from the individual pixels will be more physically accurate, and is in agreement with the overall dust mass for M 31 found by Draine et al. (2014).

However, Smith et al. (2012) find about $2.8 \times 10^7\,M_\odot$ with their higher resolution analysis, but this is likely to be related to the different approaches with SED fitting. Smith et al. effectively assumed that all emission above 100 μm originates from dust heated by a single source, whereas we show that some of the emission above 1000 GHz originates from dust heated by star formation. The Smith et al. (2012) dust temperatures will therefore be higher, which will bias the resulting dust masses lower.

We have also fitted the data using a variable spectral index. The results of these fits for both the full and rescaled SEDs are shown in Fig. 12. The behaviour of the temperature and spectral index are somewhat different in these two situations. When fitting the entire SED, the resulting temperature distribution is much more uniform than for the fixed $\beta_{\rm dust}$ case, whilst the spectral index decreases with galactocentric distance. The same behaviour is still evident when the rescaled SEDs are fitted; however, it is less significant. This helps explain some of the differences between our analysis and that using the *Herschel* data described in Smith et al. (2012), where the entire SED has been fitted without taking into account the heating mechanism. The behaviour of flatter spectral indices further out from the galactic centre was noted by Smith et al. (2012), and has also been seen in our Galaxy (Paradis et al. 2012b; Planck Collaboration XI 2014). The fitted spectral indices are steep, with a range of 1.8–2.5 for M 31 both here and in Smith et al. (2012); in comparison, our Galaxy has much flatter spectral indices of 1.4–1.8 (Planck Collaboration XI 2014).

We plot the temperatures vs. $\beta_{\rm dust}$ for both the entire SED and the rescaled SED in Fig. 13. There is a systematic shift towards colder temperatures of about 9% when fitting the rescaled SED compared with the entire SED, while the $\beta_{\rm dust}$ distribution steepens slightly from an average of 1.80 for the entire SED to 1.70 for the rescaled SED. It is well known that there is a significant degeneracy present when both the temperature and spectral index are allowed to vary (e.g., see Shetty et al. 2009; Galametz et al. 2012; Juvela & Ysard 2012), but we do not see evidence for this here.

We have also carried out this analysis using the `NILC` CMB subtraction and find very similar results, with differences primarily in the outermost pixels where the signal is weaker compared to the CMB. As seen in Sect. 5, the colour ratio analysis is negligibly affected by the different CMB subtraction; the SED fitting is more sensitive to differences in the 353 GHz (850 μm) flux density. For the fixed β case, the dust mass changes by an average of 0.37σ, and a maximum of 1.8σ, and the temperature changes by an average of 0.4σ and a maximum of 2.6σ, with the largest changes being at high galactocentric distances. Repeating this analysis using the combination of 24 μm and FUV data to trace the star formation also does not have a significant effect, with dust temperature estimates from the rescaled SEDs changing by a maximum of 1.6 K.

7. Integrated SED

We use aperture photometry to construct an integrated spectrum of M 31 as a whole, using the same code developed for Planck Collaboration XX (2011) and Planck Collaboration Int. XV (2014), with modifications to enable us to have an elliptical aperture. The aperture is shown in Fig. 14. We use an inner radius of 100′, and a background annulus between 100′ and 140′, with a ratio of the major to minor axes of 0.7 and an angle of 45°. We convolve the data set (in `HEALPix` format) to 1° resolution prior to extracting the flux densities to have a matched resolution data set across all frequencies, which allows us to accurately compile the measured flux densities across the spectrum. The measured flux densities for M 31 at the various frequencies (prior to colour correction) are listed in Table 3.

We use a Bayesian Markov chain Monte Carlo (MCMC) technique, as described by Planck Collaboration XVI (2011),

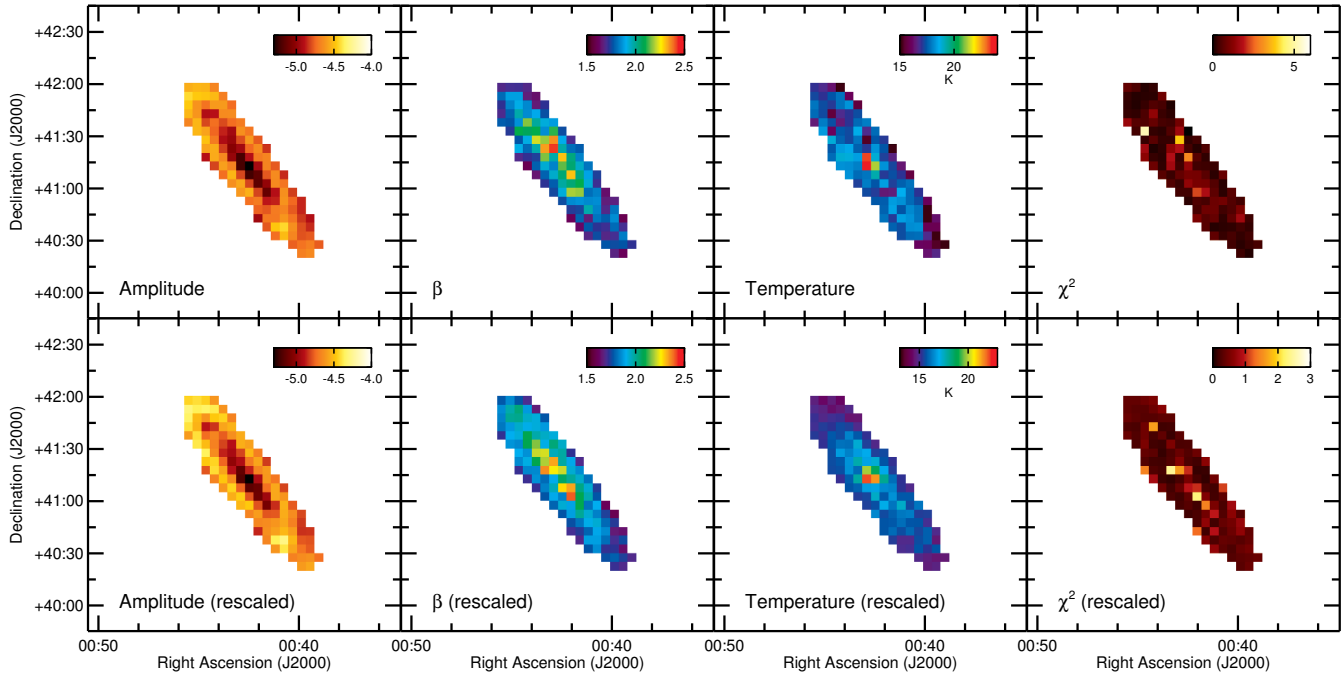

Fig. 12. Results from allowing $\beta_{\rm dust}$ to vary. *Top*: fitting for the entire SED. *Bottom*: fitting to the rescaled SED (i.e., only the dust component that is heated by the stellar population). *Left to right*: the fitted dust optical depth, spectral index, temperature, and reduced χ^2. Note the difference in morphology for the dust temperature and indices.

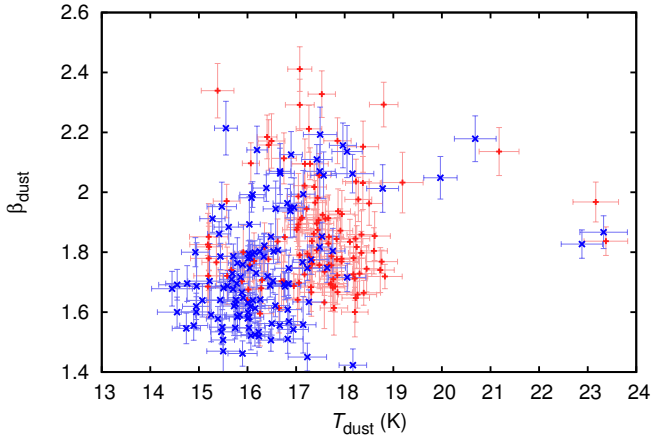

Fig. 13. $T_{\rm dust}$ vs. $\beta_{\rm dust}$ for the entire SED (red plus symbols) and the rescaled SED (blue crosses). There is a systematic shift to lower dust temperatures with the rescaled SEDs, while the distribution of $\beta_{\rm dust}$ does not change as much.

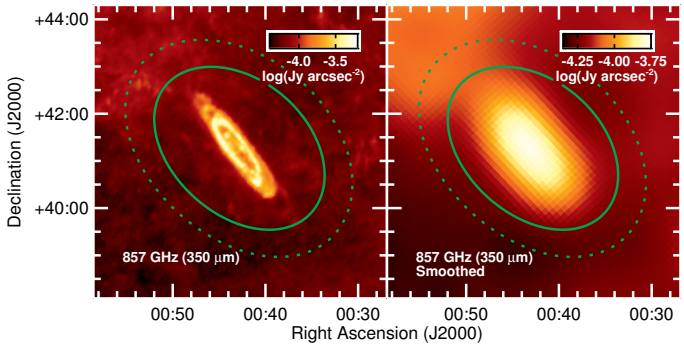

Fig. 14. Aperture used to extract the total emission from M 31, superimposed on the raw (*left*) and 1°-convolved (*right*) 857 GHz map.

to fit the multiple components of the spectrum between 0.408 and 3000 GHz (73.4 cm and 100 μm) via

$$S(\nu) = A_{\rm sync}\nu^{\alpha} + S_{\rm ff}(\nu) + S_{\rm AME}(\nu) + S_{\rm dust}(\nu) + S_{\rm cmb}, \quad (6)$$

where the synchrotron emission is characterized by a power law with amplitude $A_{\rm sync}$ and index α. $S_{\rm dust}$ is given by a single modified blackbody spectrum as

$$S_{\rm dust}(\nu) = 2\,h\,\frac{\nu^3}{c^2}\,\frac{1}{e^{h\nu/kT_{\rm dust}}-1}\,\tau_{250}\left(\frac{\nu}{250\,\mu{\rm m}}\right)^{\beta_{\rm dust}}\Omega, \quad (7)$$

with free parameters τ_{250}, $T_{\rm dust}$ and $\beta_{\rm dust}$. Note that this is fitted to the measured SED, rather than a rescaled SED as in previous sections.

The free-free flux density, $S_{\rm ff}$, is calculated from the brightness temperature, $T_{\rm ff}$, based on the optical depth, $\tau_{\rm ff}$, using

$$S_{\rm ff} = \frac{2kT_{\rm ff}\Omega\nu^2}{c^2}, \quad (8)$$

where Ω is the solid angle, ν is the frequency,

$$T_{\rm ff} = T_{\rm e}(1-{\rm e}^{-\tau_{\rm ff}}), \quad (9)$$

and the optical depth, $\tau_{\rm ff}$, is given by

$$\tau_{\rm ff} = 5.468\times10^{-2}\,T_{\rm e}^{-1.5}\,\nu^{-2}\,{\rm EM}\,g_{\rm ff}, \quad (10)$$

in which the Gaunt factor is approximated by (Draine 2011)

$$g_{\rm ff} = \ln\left(\exp\left[5.960 - \frac{\sqrt{3}}{\pi}\ln(Z_i\,\nu_9\,T_4^{-3/2})\right] + e\right), \quad (11)$$

where $e = 2.71828$. We assume a fixed electron temperature of $T_{\rm e} = 8000$ K, which is a typical value from our Galaxy, and fit for the emission measure (EM).

Table 3. Flux densities for the integrated spectrum from aperture photometry.

Survey	ν [GHz]	λ [mm]	Flux density [Jy]
Haslam	0.408	734	23.1 ± 4.5
Dwingeloo	0.82	365	13.0 ± 2.4
Reich	1.42	214	7.5 ± 0.8
WMAP	22.8	13	2.09 ± 0.10
Planck	28.4	10.5	2.05 ± 0.11
WMAP	33.0	9.0	1.88 ± 0.14
WMAP	40.7	7.4	1.73 ± 0.18
Planck	44.1	6.8	1.31 ± 0.21
WMAP	60.7	4.9	2.90 ± 0.38
Planck	70.4	4.3	3.27 ± 0.51
WMAP	93.5	3.2	4.32 ± 0.78
Planck	100	3.0	7.3 ± 1.2
Planck	143	2.1	18.2 ± 1.5
Planck	217	1.38	76.0 ± 8.2
Planck	353	0.85	298 ± 13
Planck	545	0.55	1018 ± 104
Herschel	600	0.50	1290 ± 130
Planck	857	0.35	3050 ± 310
Herschel†	857	0.35	3040 ± 310
Herschel	1200	0.25	5840 ± 770
COBE-DIRBE†	1249	0.24	5700 ± 770
Herschel	1874	0.16	6900 ± 900
COBE-DIRBE	2141	0.14	7300 ± 1000
COBE-DIRBE†	2997	0.10	3600 ± 500
IRAS†	2997	0.10	3330 ± 440
Herschel	2998	0.10	2960 ± 390
COBE-DIRBE†	4995	0.06	710 ± 100
IRAS†	4995	0.06	750 ± 100
IRAS†	12 000	0.025	134 ± 17
IRAS†	25 000	0.012	184 ± 24

Notes. The flux densities have not been colour-corrected. Values marked with † were not included in the fit.

We also fit for anomalous microwave emission using

$$S_{\rm AME} = A_{\rm AME}\, j(\nu)\, \Omega, \tag{12}$$

where we use a warm ionized medium (WIM) model for $j(\nu)$ calculated from SPDUST (Ali-Haïmoud et al. 2009; Silsbee et al. 2011). The amplitude $A_{\rm AME}$ has units of aperture area times the column density (Sr cm^{-2}).

The CMB is fitted using the differential of a blackbody at $T_{\rm CMB} = 2.7255$ K (Fixsen 2009):

$$S_{\rm cmb} = \left(\frac{2k\Omega\nu^2}{c^2}\right)\Delta T_{\rm CMB}, \tag{13}$$

where $\Delta T_{\rm CMB}$ is the CMB fluctuation temperature in thermodynamic units. We do not attempt to remove CMB from the maps before carrying out the aperture photometry and analysis of the SED. The CMB amplitude can be either negative or positive.

The best-fit model from the Bayesian analysis is shown in Fig. 15, with the mean fit parameters given Table 4. The samples from the SED likelihood function are shown in Fig. 16. We find that there is a good fit across all of the frequencies ($\chi^2 = 15.4$ with $N_{\rm d.o.f.} = 14$), with steep spectrum synchrotron emission dominating the radio frequencies, a significant amount of free-free emission dominating the flux densities between 10 and 50 GHz, along with CMB at frequencies around 100 GHz, and cold thermal dust emission at higher frequencies. We report results here using the 2013 *Planck* data set. We have repeated this analysis with the 2015 *Planck* data (Planck Collaboration I 2015), and find no significant differences.

Table 4. Best-fitting parameters for the integrated spectrum from the Bayesian analysis.

Parameter	Value
τ_{250}	$(1.2 \pm 0.2) \times 10^{-5}$
$\beta_{\rm dust}$	1.62 ± 0.11
$T_{\rm dust}$ [K]	18.2 ± 1.0
EM [cm^{-6} pc]	1.8 ± 1.3
$\Delta T_{\rm CMB}$ [K]	$(1.7 \pm 1.0) \times 10^{-6}$
$A_{\rm synch}$ [Jy]	9.5 ± 1.1
$\alpha_{\rm synch}$	-0.92 ± 0.16
$A_{\rm AME}$ [Sr cm^{-2}]	$(7.7 \pm 3.3) \times 10^{16}$
χ^2	15.4
$N_{\rm d.o.f.}$	14

We find that the synchrotron emission in the aperture has an amplitude at 1 GHz of 9.5 ± 1.1 Jy and a steep spectrum with a power-law index of ($\alpha = -0.92 \pm 0.16$), which is in the range of typical synchrotron spectral indices for normal galaxies of about −0.85 (e.g., Condon 1992; Niklas et al. 1997, but these may include a contribution from a thermal component, see Peel et al. 2011). This is poorly constrained as synchrotron is not a significant component in the fit at the *Planck* and WMAP frequencies[7]. This emission includes both compact and diffuse emission from M 31 that is within the aperture, as well as foreground emission from our Galaxy and emission from bright quasars behind M 31 (particularly at the lowest frequencies) – although faint AGN, being more numerous, should statistically cancel out, as there should be as many of them in the background annulus as in the aperture. Bright compact sources are particularly visible in the high-resolution surveys of M 31, as described by Graeve et al. (1981). Berkhuijsen et al. (2003) use a compilation of source-subtracted measurements of M 31 to measure the integrated flux densities out to 16 kpc and find significantly lower flux densities than the fit here. For example, they quote (11.20 ± 0.81) Jy of emission at 408 MHz from Pooley (1969) compared to the (23.1 ± 4.5) Jy that we find here from the Haslam et al. (1981) 408 MHz map; in contrast Graeve et al. (1981) find a much higher flux density of (63.7±6.7) Jy when the "halo" emission around M 31 (which comes from point sources and a Galactic spur) is also considered. This difference is therefore presumably due to foreground emission and extragalactic sources in the aperture.

A significant amount of free-free emission is needed to account for the flux density detected in the lower *Planck* and WMAP bands; the model fit implies that a large fraction of the flux density seen at frequencies of 20–60 GHz is caused by free-free emission. Similar results have been seen in other nearby galaxies. For example, Peel et al. (2011) also found that a significant amount of free-free emission was needed to give realistic star formation rates for Messier 82, NGC 4945, and NGC 253. Free-free emission scales linearly with the star-formation rate (see e.g., Murphy et al. 2011). Azimlu et al. (2011) have calculated the star formation rate based on Hα imaging and find it to be 0.44 $M_\odot\,{\rm yr}^{-1}$, which is higher than the (0.25 ± 0.05) $M_\odot\,{\rm yr}^{-1}$ found by Ford et al. (2013) using ultraviolet and 24 μm data. The SFR of (0.36 ± 0.14) $M_\odot\,{\rm yr}^{-1}$estimated

[7] Additional data at frequencies around 5–15 GHz, e.g., by C-BASS (King et al. 2010), would be required to see whether the synchrotron radiation is steepening or flattening at high frequencies, see e.g., Strong et al. (2011) and Peel et al. (2012).

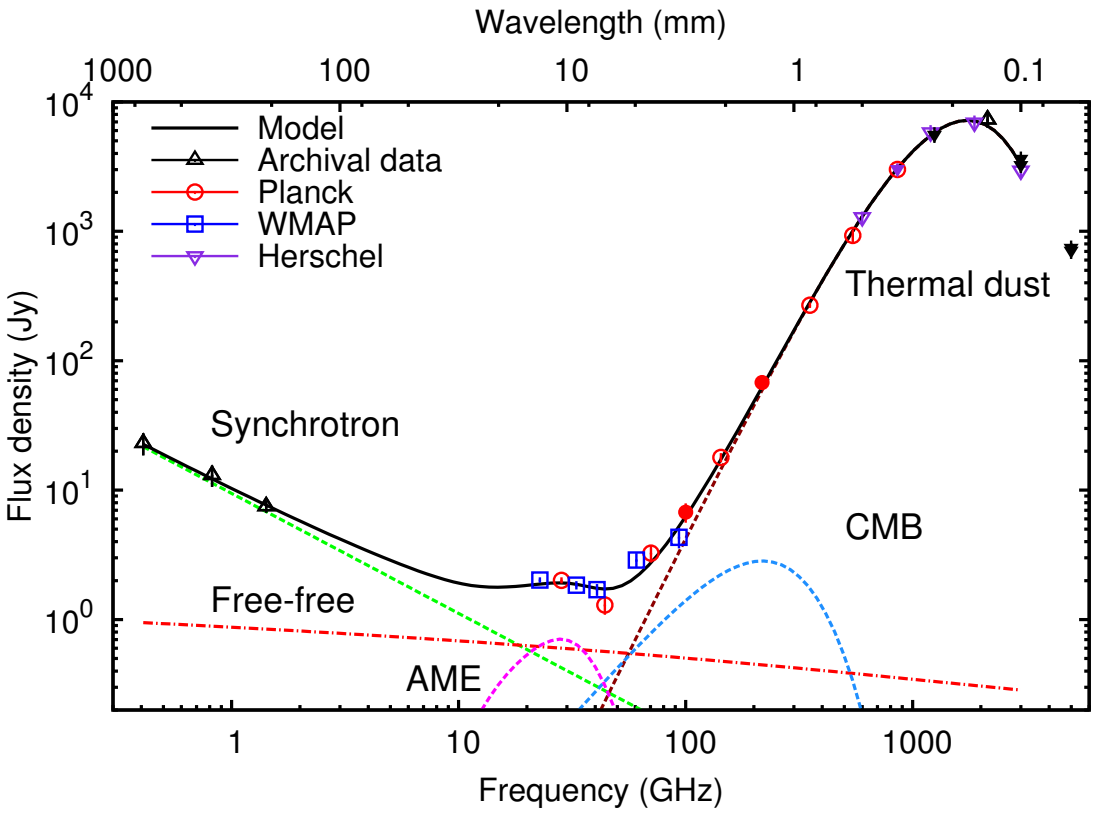

Fig. 15. The integrated SED from radio to far-infrared, with the best-fit model from Bayesian analysis (see Sect. 7). Data points are from WMAP (blue), *Planck* (red), *Herschel* (purple) and other archival data (black). Filled points represent data that were not included in the fit. The best fit is shown in black; the green line shows the synchrotron fit, the red line shows the free-free emission, the magenta curve shown the AME, the dark red line shows the thermal dust, and the light blue line shows the CMB.

by Xu & Helou (1996) using IRAS data of M 31 lies in between these. Star formation rates can be calculated from the EM (and flux densities) that we are fitting for here using the formulae from Condon (1992). In our standard model, without applying any priors, we find an EM of $(1.8 \pm 1.3)\,\mathrm{cm}^{-2}\,\mathrm{pc}$ ($\approx$0.7 Jy at 10 GHz), which equates to an SFR of $\approx 0.12\,M_{\odot}\,\mathrm{yr}^{-1}$; this is substantially lower than the SFR from Ford et al. (2013) and Xu & Helou (1996), and lower than the SFR from Hα.

The Bayesian analysis gives an AME amplitude of $(7.7 \pm 3.3) \times 10^{16}\,\mathrm{Sr\,cm}^{-2}$, which is a 2.3 σ marginal detection of the presence of AME in M 31. We can estimate the amount of AME that we might expect based on observations of anomalous emission in our Galaxy (Todorović et al. 2010; Alves et al. 2012). The ratio between AME at 30 GHz and thermal dust emission as seen by IRAS at 100 μm is expected to be about 1:3000 in flux density, although there is a considerable amount of scatter in this number (see Planck Collaboration Int. XV 2014; additionally Planck Collaboration XVII 2011 found a ratio of approximately 1:2000 for the Small Magellanic Cloud) and it is sensitive to dust temperature (Tibbs et al. 2012). As we find (3330 ± 440) Jy at 100 μm, this implies that the 30 GHz AME emission should be (1.11 ± 0.15) Jy (with the uncertainty only coming from the 100 μm flux density, not from the ratio). At 30 GHz we find an AME flux of (0.7$\pm$0.3) Jy, which is comparable with the expectation based on the AME level seen in our Galaxy. The results are also compatible with those for AME in other nearby galaxies (M 82, NGC 253, and NGC 4945) presented by Peel et al. (2011) and the detection of AME within only one of ten star-forming clouds observed by Murphy et al. (2010) and AMI Consortium et al. (2010) within NGC 6946. The main source of uncertainty here is the level of the free-free emission. Observations at frequencies of 5–10 GHz (e.g., a 5 GHz measurement from C-BASS, King et al. 2010; Irfan et al. 2015) would improve these constraints.

Due to the correlations between α_{sync} and EM, and EM and A_{AME}, we have tried setting Gaussian priors on the α_{sync} and EM parameters, with values of $\alpha_{\mathrm{sync}} = -0.90 \pm 0.3$, and EM = 5.0 ± 1.0. Applying both priors results in a slightly higher $\chi^2 = 18.6$, with $\alpha_{\mathrm{sync}} = -1.02 \pm 0.13$, EM = 4.0 ± 0.9 and $A_{\mathrm{AME}} = (4 \pm 2) \times 10^{16}\,\mathrm{Sr\,cm}^{-6}\,\mathrm{pc}$, and there is a negligible effect on the mean values of the other fit parameters (changes are less than 1σ). As such, we have conservatively used wide uniform priors for our canonical model here.

We find that the thermal dust emission can be well characterized with a single modified blackbody spectrum, with an effective temperature of (18.2 ± 1.0) K, a spectral index $\beta_{\mathrm{dust}} = 1.62 \pm 0.11$ and an optical depth of $(1.2 \pm 0.2) \times 10^{-5}$. The overall cold temperature of the dust agrees with the *Herschel* observations, which found an average temperature of (18.1 ± 0.2) K (Fritz et al. 2012). This is higher than the temperature of (16.96 ± 0.13) K found in Sect. 6.3. The higher temperature obtained when allowing β_{dust} to vary is an expected consequence of the degeneracy between temperature and β_{dust} (Shetty et al. 2009). The spectral index is lower than would have been expected from the statistical β_{dust}–T_{dust} relation seen in nearby galaxies in Planck Collaboration XVI (2011), where at this temperature $\beta_{\mathrm{dust}} > 2$ would have been expected. It is, however, higher than the values seen in the LMC and SMC of around 1.5 and 1.2, respectively (Planck Collaboration XVII 2011), and is comparable to the typical values of β_{dust} seen in our Galaxy

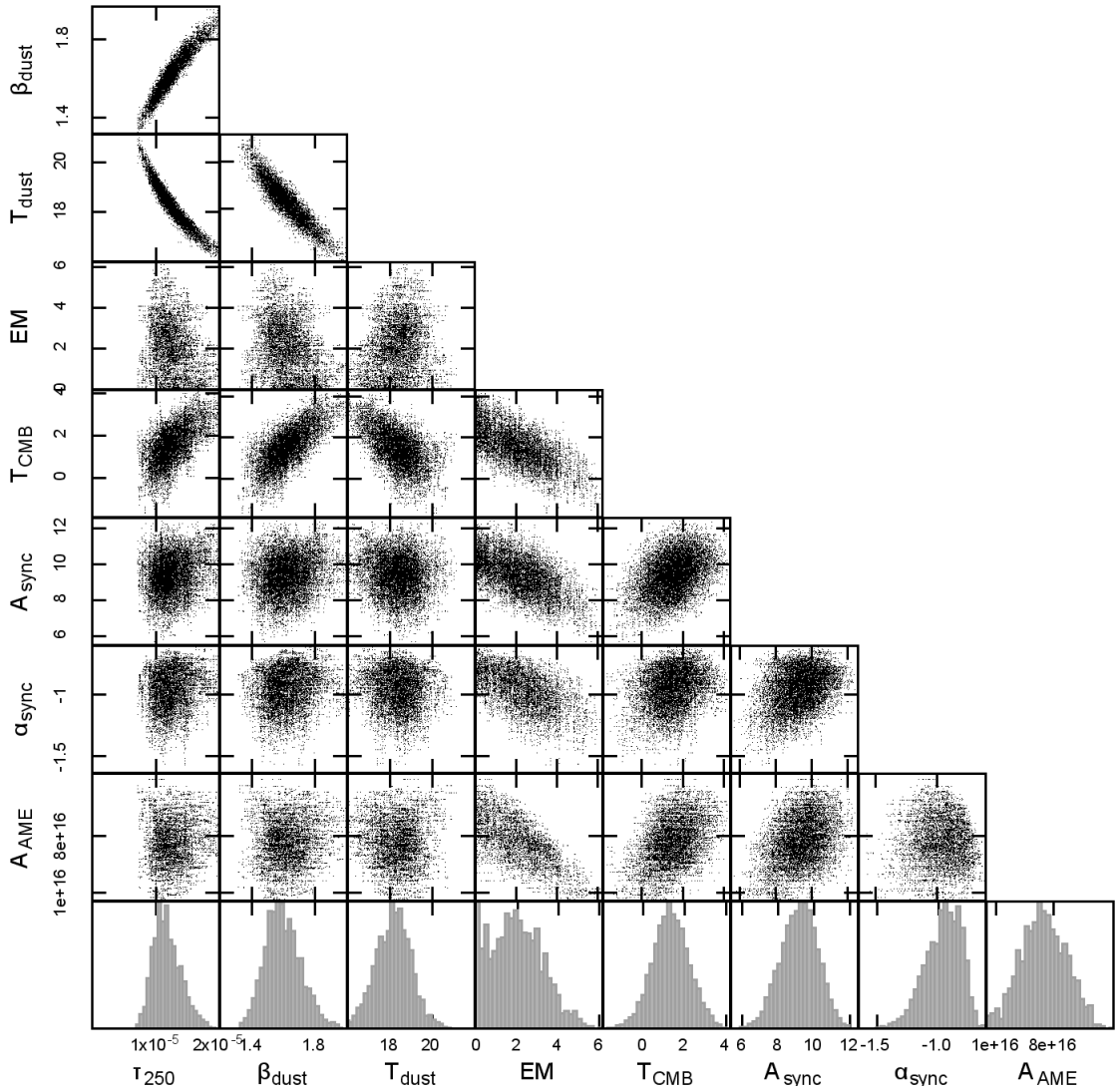

Fig. 16. The samples from the SED likelihood function for the Bayesian analysis. The bottom row shows the one-dimensional (marginalized) posterior for the parameters, with the other rows showing all of the two-dimensional marginal distributions.

Planck Collaboration Int. XVII (2014). We note that it is surprising how well the single temperature modified blackbody fits the data. Even though this function does not replicate the emission at <100 μm from small dust grains that are stochastically heated by the diffuse ISRF, it still appears to be a good model for the overall emission from a galaxy and can provide a characteristic temperature for the large dust grains.

A positive differential CMB contribution is found, with an amplitude of $(1.7 \pm 1.0) \times 10^{-6}$ K. That this signal is positive is not too surprising, given the presence of the large positive CMB anisotropy seen in Fig. 1. Planck Collaboration XVII (2011) also found positive residual CMB contributions for the LMC and SMC, and Planck Collaboration Int. XV (2014) found that AME sources preferentially had larger CMB contributions to their spectra. The CMB amplitude is degenerate with the dust spectral index, so a flattening of this spectral index (e.g., as seen in our Galaxy by Planck Collaboration Int. XIV 2014) would reduce the contribution from the CMB in this spectrum; the positive CMB fluctuation may be accounting for a small excess of emission in the range 100–300 GHz. Further investigation of the CMB contribution would be needed to identify whether that is the case here or not.

The 100 and 217 GHz bands of *Planck* are particularly contaminated with ^{12}CO [8], and consequently these bands were not included in the fit. Using the unit conversion coefficient estimates of the ^{12}CO contamination of the *Planck* maps from Planck Collaboration (2013) of (14.78 ± 0.21) and $(45.85 \pm 0.11)\,\mu\mathrm{K_{CMB}}\,[\mathrm{K\,km\,s^{-1}}]^{-1}$ at 100 and 217 GHz, respectively, and the sum of the emission in the Nieten et al. (2006) CO map of 109 481 K km s^{-1}, we estimate that within the elliptical aperture centred on M 31, the *Planck* maps should contain a total of 0.58 Jy of CO emission at 100 GHz and 3.6 Jy at 217 GHz. These estimates agree within a factor of two with measurements of the CO contamination given by the residuals after subtracting the thermal dust model. At 100 GHz, there is a difference of (-0.08 ± 1.16) Jy between the data and the model fit, corresponding to 1.3% of the flux density measured at that frequency. At 217 GHz it is (-2.2 ± 8.2) Jy, or 3.5%. In both

[8] ^{13}CO also emits in these frequency bands with a similar unit conversion coefficient, but the ^{13}CO line amplitudes are a factor of around 10 fainter than the ^{12}CO amplitudes (e.g., Allen et al. 1995); ^{12}CO/^{13}CO ratios are expected to be similar in M 31 to Galactic values, since ^{13}CO is produced through hot-bottom burning in asymptotic giant branch stars (Herwig 2005).

cases, the uncertainties in the measurement are larger than the expected level of CO from M 31.

8. Conclusions

Planck has clearly detected emission from the Andromeda galaxy across all of its frequency bands, and the High Frequency Instrument has mapped out the emission at 5′ scales. Multiple spiral arm features are seen to both the north and south of the galaxy, with the 10 kpc ring clearly detected down to 100 GHz, and additional spiral arm structures extending out to 26 kpc from the nucleus. Knots of emission at various points within M 31 can also seen in the *Planck* data.

Smoothing the *Planck* data to a common resolution and combining it with ancillary data, has provided a powerful probe of the dust properties. By looking at colour ratio plots, it can be seen that the dust observed at the longest wavelengths ($\gtrsim$0.3 mm) is heated by the diffuse stellar population (as traced by the stellar emission at 3.6 μm), whilst the dust observed at higher frequencies is heated by more local features (as traced by the star formation emission at 24 μm). Throughout the *Planck* frequency range the dust emission is primarily from dust heated by the diffuse stellar population rather than star formation.

By fitting a single modified thermal dust spectrum to individual pixels, the variations in dust mass and temperature across M 31 can be seen. When a fixed $\beta_{\rm dust} = 2$ is used and the SED is rescaled to include only the component that is attributable to the dust heated by the old stellar population, then the dust temperature is inversely proportional to the galactocentric distance. When the spectral index is allowed to vary, then we recover values of $\beta_{\rm dust} \approx 2$ when only fitting the rescaled pixel SEDs. When we fit the unscaled pixel SEDs using a variable $\beta_{\rm dust}$ (see Sect. 6.3), we find that the variations in $\beta_{\rm dust}$ could be due to variations in the relative amplitudes of emission from hotter dust heated by star formation and cooler dust heated by the old stellar population rather than variations in the physical emissivity of the dust grains.

Using aperture photometry, the integrated spectrum of all of the emission from M 31 has been measured. This spectrum is well fitted with a combination of free-free, CMB and cold thermal dust emission. Overall, the fitted dust temperature is reasonably cold, at (18.2 ± 1.0) K, with a spectral index of 1.62 ± 0.11. The significant amount of free-free emission corresponds to a star formation rate of around 0.12 $M_\odot\,{\rm yr}^{-1}$. We find a 2.3σ marginal detection of AME in M 31, with an amplitude of (0.7 ± 0.3) Jy at 30 GHz, which is comparable to the expected level of around 1 Jy from measurements of the ratio of AME to thermal dust emission in our Galaxy.

Acknowledgements. We thank M. Haas for providing a copy of the reduced 170 μm data from ISO, P. Barmby for providing the *Spitzer* IRAC 3.6 μm data, L. Chemin for providing the H I map from DRAO, J. Fritz, M. Smith and others in the HELGA collaboration for providing a copy of the *Herschel* data, S. Viaene for providing a copy of the foreground star-subtracted GALEX map, and A. Richards for assistance with the CO data. We acknowledge the use of the Legacy Archive for Microwave Background Data Analysis (LAMBDA); support for LAMBDA is provided by the NASA Office of Space Science. This research has made use of the NASA/IPAC Extragalactic Database (NED) which is operated by the Jet Propulsion Laboratory, California Institute of Technology, under contract with the National Aeronautics and Space Administration. Some of the results in this paper have been derived using the `HEALPix` package. The research leading to these results has received funding from the European Research Council under the European Union's Seventh Framework Programme (FP7/2007-2013)/ERC grant agreement No. 307209, as well as funding from an STFC Consolidated Grant (No. ST/L000768/1). The development of *Planck* has been supported by: ESA; CNES and CNRS/INSU-IN2P3-INP (France); ASI, CNR, and INAF (Italy); NASA and DoE (USA); STFC and UKSA (UK); CSIC, MICINN, JA, and RES (Spain); Tekes, AoF, and CSC (Finland); DLR and MPG (Germany); CSA (Canada); DTU Space (Denmark); SER/SSO (Switzerland); RCN (Norway); SFI (Ireland); FCT/MCTES (Portugal); and PRACE (EU). A description of the Planck Collaboration and a list of its members, including the technical or scientific activities in which they have been involved, can be found at http://www.sciops.esa.int/index.php?project=planck&page=Planck_Collaboration

Appendix A: Comparison data sets

As described in Sect. 3.1, we make use of the following data sets for comparison purposes.

We use the IRAS data at 12, 25, 60, and 100 μm in the form of the improved reprocessing of the IRAS survey (IRIS) (Miville-Deschênes & Lagache 2005)[9], which is based on the IRAS Sky Survey Atlas (Wheelock et al. 1994), but has improved processing to achieve a higher resolution of 3.′8–4.′3, depending on the wavelength.

We make use of the ISO 175 μm data from Haas et al. (1998, priv. comm.), which has 1.′3 resolution. This data set (along with the low-resolution COBE-DIRBE data) sits in the the frequency gap between *Planck* and *Spitzer*. As the version of these data that we use has not been pre-calibrated, we calibrate them such that the sum of the pixels adds up to the overall flux density of 7900 Jy within the area surveyed by ISO, as reported in Haas et al. (1998). We caution that the ISO data are not well sampled, meaning that some of the large-scale emission will be missing from these data, which may result in underestimates of the flux densities in the following analysis. We do not fit to this data; instead we include it for comparison purposes.

Several maps of H I emission from M 31 exist (e.g., Unwin 1983; Chemin et al. 2009; Braun et al. 2009). We make use of the recent H I emission map from Chemin et al. (2009) to trace the gas within M 31. This map was constructed using a combination of interferometric and single dish data using the Synthesis Telescope and the 26-m Telescope at the Dominion Radio Astrophysical Observatory (DRAO). This combination means that the map has 22″ resolution, whilst not resolving out extended emission, and it also covers the full extent of M 31, including the outermost spiral arms. Although the original map is contaminated by H I emission from our Galaxy at the same frequencies as that from part of M 31, this has been removed by Chemin et al. (2009). We flatten the image cube to an intensity map (by summing up the brightness temperature over the frequency channels within a spatial pixel), convolve it to 5′, and resample it to match the *Planck* data set using `Aladin`[10] (Bonnarel et al. 2000) to take into account differences in the coordinate projection systems used.

Finally, we also make use of the ^{12}CO $J = 1 \rightarrow 0$ map of M 31 from Nieten et al. (2006), which is constructed from 23″ resolution observations with the IRAM 30-m telescope. This map covers the 10 kpc ring structure, but does not include the outermost spiral arm structures. We use this map to compare with the *Planck* data in the bands that have been contaminated with CO emission, particularly for the integrated spectrum in Sect. 7. The data (downloaded from NED) were reprojected using `AIPS` prior to being smoothed and repixelised.

Appendix B: Compact sources in and around M 31

Following from Sect. 4, we provide some comments about objects in the field around M 31 that are visible in Figs. 2 and 3,

[9] http://www.cita.utoronto.ca/~mamd/IRIS/
[10] http://aladin.u-strasbg.fr/

and features of M 31 that are included in the ERCSC and PCCS catalogues.

M110/NGC205 is clearly detected at 857 GHz (350 μm; position: $00^h40^m22.1^s$, +41°41′7″ J2000, distance (809 ± 24) kpc, McConnachie et al. 2005, "F6" in Fig. 3). This dwarf galaxy has also been seen in thermal dust emission by *Spitzer* and *Herschel* (De Looze et al. 2012), and it is known to be surprisingly dust-rich. Messier 32, which is at position $00^h42^m41.8^s$, +40°51′55″, is not detected. This is because it is faint at these frequencies (it has been measured by ISO to be less than 0.27 Jy at 200 μm, Temi et al. 2004), and it is also very close to the bright 10 kpc ring, which means that it is not in a clean environment to be detected with the spatial resolution of the *Planck* data.

There is also a detection of the blazar B3 0035+413 as a compact source at 28.4, 100, 143, and 217 GHz (13, 3.0, 2.1, and 1.38 mm; position $00^h38^m30^s$, +41°34′40″; marked in the left-hand panels of Fig. 3 as "B3"). The high-frequency flux density of this flat spectrum source, as measured by the One Centimetre Receiver Array at 30 GHz (10 mm), is (395 ± 20) mJy (Lowe et al. 2007), so it is unsurprising that it is seen in the *Planck* maps at these frequencies. It is not included in the *Planck* Early Release Compact Source Catalogue (ERCSC; Planck Collaboration VII 2011), since the CMB signal is much stronger than the source flux at these frequencies. It is, however, in the second *Planck* catalogue, the *Planck* Catalogue of Compact Sources (PCCS; Planck Collaboration XXVIII 2014), due to the filtering carried out prior to source extraction; it is listed there as PCCS1 100 G120.34−21.17 (DETFLUX of 350 ± 80 mJy), PCCS1 143 G120.32−21.16 (260 ± 40 mJy), and PCCS1 217 G120.28−21.16 (220 ± 40 mJy). At a redshift of 1.35, the source is not physically associated with M 31, but is just a line-of-sight coincidence.

Several bright segments of the M 31 ring structure were detected in the ERCSC at the 143 to 857 GHz (2.1 to 0.35 mm) channels. Most of these sources are flagged as EXTENDED (EXT) in the ERCSC, which indicates that under a Gaussian fit, the square root of the product of the fitted major axis and minor axis is larger than 1.5 times the beam FWHM at a given frequency. The ERCSC sources are marked in the top-right panel of Fig. 3, where they are circled at their 857 GHz (350 μm) positions, with the circles being 5′ in radius, such that they have a diameter approximately equal to twice the FWHM at the 857 GHz (350 μm) channel. Sources 2 to 5 are clearly within the star-forming ring ∼10 kpc offset from the nucleus, while source 1 belongs to the outer ring that is seen both by ISO and *Spitzer* MIPS. A much larger number of segments of the ring are included by the PCCS, with 21–32 sources detected in PCCS 217–857 GHz (1.38–0.35 mm) bands on the inner ring alone, which are marked as extended. Due to the large number of segments included in the PCCS, we do not circle them in Fig. 3.

References

Abdo, A. A., Ackermann, M., Ajello, M., et al. 2010, A&A, 523, L2
Ali-Haïmoud, Y., Hirata, C. M., & Dickinson, C. 2009, MNRAS, 395, 1055
Allen, R. J., Le Bourlot, J., Lequeux, J., Pineau des Forets, G., & Roueff, E. 1995, ApJ, 444, 157
Alves, M. I. R., Davies, R. D., Dickinson, C., et al. 2012, MNRAS, 422, 2429
AMI Consortium, Scaife, A. M. M., Nikolic, B., et al. 2010, MNRAS, 406, L45
Aniano, G., Draine, B. T., Calzetti, D., et al. 2012, ApJ, 756, 138
Azimlu, M., Marciniak, R., & Barmby, P. 2011, AJ, 142, 139
Barmby, P., Ashby, M. L. N., Bianchi, L., et al. 2006, ApJ, 650, L45
Beck, R., Berkhuijsen, E. M., & Hoernes, P. 1998, A&AS, 129, 329
Bendo, G. J., Wilson, C. D., Pohlen, M., et al. 2010, A&A, 518, L65
Bendo, G. J., Boselli, A., Dariush, A., et al. 2012a, MNRAS, 419, 1833
Bendo, G. J., Galliano, F., & Madden, S. C. 2012b, MNRAS, 423, 197
Bendo, G. J., Griffin, M. J., Bock, J. J., et al. 2013, MNRAS, 433, 3062
Bendo, G. J., Baes, M., Bianchi, S., et al. 2015, MNRAS, 448, 135
Bennett, C. L., Larson, D., Weiland, J. L., et al. 2013, ApJS, 208, 20
Berkhuijsen, E. M. 1972, A&AS, 5, 263
Berkhuijsen, E. M., Beck, R., & Hoernes, P. 2003, A&A, 398, 937
Bersanelli, M., Mandolesi, N., Butler, R. C., et al. 2010, A&A, 520, A4
Bonnarel, F., Fernique, P., Bienaymé, O., et al. 2000, A&AS, 143, 33
Boquien, M., Calzetti, D., Combes, F., et al. 2011, AJ, 142, 111
Braun, R., Thilker, D. A., Walterbos, R. A. M., & Corbelli, E. 2009, ApJ, 695, 937
Brown, R. H., & Hazard, C. 1950, Nature, 166, 901
Brown, R. H., & Hazard, C. 1951, MNRAS, 111, 357
Buat, V., & Xu, C. 1996, A&A, 306, 61
Calzetti, D., Kennicutt, Jr., R. C., Bianchi, L., et al. 2005, ApJ, 633, 871
Calzetti, D., Kennicutt, R. C., Engelbracht, C. W., et al. 2007, ApJ, 666, 870
Chemin, L., Carignan, C., & Foster, T. 2009, ApJ, 705, 1395
Condon, J. J. 1992, ARA&A, 30, 575
Dale, D. A., Gil de Paz, A., Gordon, K. D., et al. 2007, ApJ, 655, 863
Dame, T. M., Koper, E., Israel, F. P., & Thaddeus, P. 1993, ApJ, 418, 730
De Looze, I., Baes, M., Parkin, T. J., et al. 2012, MNRAS, 423, 2359
De Looze, I., Fritz, J., Baes, M., et al. 2014, A&A, 571, A69
De Paolis, F., Gurzadyan, V. G., Ingrosso, G., et al. 2011, A&A, 534, L8
De Paolis, F., Gurzadyan, V. G., Nucita, A. A., et al. 2014, A&A, 565, L3
de Vaucouleurs, G., de Vaucouleurs, A., Corwin, H. G. J., et al. 1991, Third Reference Catalogue of Bright Galaxies, vols. 1–3 (Heidelberg, New York, Berlin: Springer-Verlag)
Dennison, B., Simonetti, J. H., & Topasna, G. A. 1998, PASA, 15, 147
Devereux, N. A., & Young, J. S. 1990, ApJ, 350, L25
Draine, B. T. 2011, Physics of the Interstellar and Intergalactic Medium (Princeton University Press)
Draine, B. T., Dale, D. A., Bendo, G., et al. 2007, ApJ, 663, 866
Draine, B. T., Aniano, G., Krause, O., et al. 2014, ApJ, 780, 172
Dunne, L., Eales, S., Edmunds, M., et al. 2000, MNRAS, 315, 115
Engelbracht, C. W., Blaylock, M., Su, K. Y. L., et al. 2007, PASP, 119, 994
Engelbracht, C. W., Hunt, L. K., Skibba, R. A., et al. 2010, A&A, 518, L56
Fazio, G. G., Hora, J. L., Allen, L. E., et al. 2004, ApJS, 154, 10
Fixsen, D. J. 2009, ApJ, 707, 916
Ford, G. P., Gear, W. K., Smith, M. W. L., et al. 2013, ApJ, 769, 55
Fritz, J., Gentile, G., Smith, M. W. L., et al. 2012, A&A, 546, A34
Galametz, M., Kennicutt, R. C., Albrecht, M., et al. 2012, ApJ, 425, 763
Galliano, F., Hony, S., Bernard, J.-P., et al. 2011, A&A, 536, A88
Gordon, K. D., Rieke, G. H., Engelbracht, C. W., et al. 2005, PASP, 117, 503
Gordon, K. D., Bailin, J., Engelbracht, C. W., et al. 2006, ApJ, 638, L87
Gordon, K. D., Engelbracht, C. W., Fadda, D., et al. 2007, PASP, 119, 1019
Górski, K. M., Hivon, E., Banday, A. J., et al. 2005, ApJ, 622, 759
Graeve, R., Emerson, D. T., & Wielebinski, R. 1981, A&A, 98, 260
Groves, B., Krause, O., Sandstrom, K., et al. 2012, MNRAS, 426, 892
Haas, M., Lemke, D., Stickel, M., et al. 1998, A&A, 338, L33
Habing, H. J., Miley, G., Young, E., et al. 1984, ApJ, 278, L59
Haslam, C. G. T., Klein, U., Salter, C. J., et al. 1981, A&A, 100, 209
Haslam, C., Stoffel, H., Salter, C. J., & Wilson, W. E. 1982, A&AS, 47, 1
Hauser, M. G., Arendt, R. G., Kelsall, T., et al. 1998, ApJ, 508, 25
Helou, G., Roussel, H., Appleton, P., et al. 2004, ApJS, 154, 253
Herschel Space Observatory 2013, PACS Observer's Manual, http://herschel.esac.esa.int/Docs/PACS/html/pacs_om.html
Herwig, F. 2005, ARA&A, 43, 435
Hildebrand, R. H. 1983, QJRAS, 24, 267
Hoernes, P., Berkhuijsen, E. M., & Xu, C. 1998, A&A, 334, 57
Irfan, M. O., Dickinson, C., Davies, R. D., et al. 2015, MNRAS, 448, 3572
Juvela, M., & Ysard, N. 2012, A&A, 541, A33
Kennicutt, Jr., R. C., Hao, C.-N., Calzetti, D., et al. 2009, ApJ, 703, 1672
King, O. G., Copley, C., Davies, R., et al. 2010, in Millimeter, Submillimeter, and Far-Infrared Detectors and Instrumentation for Astronomy V, Proc. SPIE 7741, 77411I
Kirk, J. M., Gear, W. K., Fritz, J., et al. 2015, ApJ, 798, 58
Koper, E., Israel, F. P., Dame, T. M., & Thaddeus, P. 1991, ApJ, 383, L11
Lamarre, J., Puget, J., Ade, P. A. R., et al. 2010, A&A, 520, A9
Leahy, J. P., Bersanelli, M., D'Arcangelo, O., et al. 2010, A&A, 520, A8
Leroy, A. K., Walter, F., Brinks, E., et al. 2008, AJ, 136, 2782
Li, A., & Draine, B. T. 2001, ApJ, 554, 778
Lonsdale Persson, C. J., & Helou, G. 1987, ApJ, 314, 513
Lowe, S. R., Gawroński, M. P., Wilkinson, P. N., et al. 2007, A&A, 474, 1093
Lu, N., Helou, G., Werner, M. W., et al. 2003, ApJ, 588, 199
Lutz, D. 2012, PACS photometer point spread function, Version 2.0 (Herschel Science Centre)
Mandolesi, N., Bersanelli, M., Butler, R. C., et al. 2010, A&A, 520, A3
McConnachie, A. W., Irwin, M. J., Ferguson, A. M. N., et al. 2005, MNRAS, 356, 979

Mennella, A., Bersanelli, M., Butler, R. C., et al. 2011, A&A, 536, A3
Mentuch, E., Abraham, R. G., Glazebrook, K., et al. 2009, ApJ, 706, 1020
Mentuch, E., Abraham, R. G., & Zibetti, S. 2010, ApJ, 725, 1971
Miville-Deschênes, M.-A., & Lagache, G. 2005, ApJS, 157, 302
Murphy, E. J., Helou, G., Condon, J. J., et al. 2010, ApJ, 709, L108
Murphy, E. J., Condon, J. J., Schinnerer, E., et al. 2011, ApJ, 737, 67
Natale, G., Popescu, C. C., Tuffs, R. J., et al. 2015, MNRAS, 449, 243
Nieten, C., Neininger, N., Guélin, M., et al. 2006, A&A, 453, 459
Niklas, S., Klein, U., & Wielebinski, R. 1997, A&A, 322, 19
Paradis, D., Dobashi, K., Shimoikura, T., et al. 2012a, A&A, 543, A103
Paradis, D., Paladini, R., Noriega-Crespo, A., et al. 2012b, A&A, 537, A113
Peel, M. W., Dickinson, C., Davies, R. D., Clements, D. L., & Beswick, R. J. 2011, MNRAS, 416, L99
Peel, M. W., Dickinson, C., Davies, R. D., et al. 2012, MNRAS, 424, 2676
Planck Collaboration I. 2011, A&A, 536, A1
Planck Collaboration II. 2011, A&A, 536, A2
Planck Collaboration VII. 2011, A&A, 536, A7
Planck Collaboration VIII. 2011, A&A, 536, A8
Planck Collaboration IX. 2011, A&A, 536, A9
Planck Collaboration X. 2011, A&A, 536, A10
Planck Collaboration XI. 2011, A&A, 536, A11
Planck Collaboration XII. 2011, A&A, 536, A12
Planck Collaboration XIII. 2011, A&A, 536, A13
Planck Collaboration XIV. 2011, A&A, 536, A14
Planck Collaboration XV. 2011, A&A, 536, A15
Planck Collaboration XVI. 2011, A&A, 536, A16
Planck Collaboration XVII. 2011, A&A, 536, A17
Planck Collaboration XVIII. 2011, A&A, 536, A18
Planck Collaboration XIX. 2011, A&A, 536, A19
Planck Collaboration XX. 2011, A&A, 536, A20
Planck Collaboration XXI. 2011, A&A, 536, A21
Planck Collaboration XXII. 2011, A&A, 536, A22
Planck Collaboration XXIII. 2011, A&A, 536, A23
Planck Collaboration XXIV. 2011, A&A, 536, A24
Planck Collaboration XXV. 2011, A&A, 536, A25
Planck Collaboration XXVI. 2011, A&A, 536, A26
Planck Collaboration 2013, The Explanatory Supplement to the Planck 2013 results, http://pla.esac.esa.int/pla/index.html (ESA)
Planck Collaboration I. 2014, A&A, 571, A1
Planck Collaboration II. 2014, A&A, 571, A2
Planck Collaboration VI. 2014, A&A, 571, A6
Planck Collaboration XI. 2014, A&A, 571, A11
Planck Collaboration XII. 2014, A&A, 571, A12
Planck Collaboration XIII. 2014, A&A, 571, A13
Planck Collaboration XXVIII. 2014, A&A, 571, A28
Planck Collaboration Int. XIV. 2014, A&A, 564, A45
Planck Collaboration Int. XV. 2014, A&A, 565, A103
Planck Collaboration Int. XVII. 2014, A&A, 566, A55
Planck Collaboration Int. XXIX. 2014, A&A, submitted [arXiv:1409.2495]
Planck Collaboration I. 2015, A&A, submitted [arXiv:1502.01582]
Planck HFI Core Team. 2011a, A&A, 536, A4
Planck HFI Core Team. 2011b, A&A, 536, A6
Pooley, G. G. 1969, MNRAS, 144, 101
Popescu, C. C., Tuffs, R. J., Dopita, M. A., et al. 2011, A&A, 527, A109
Prescott, M. K. M., Kennicutt, Jr., R. C., Bendo, G. J., et al. 2007, ApJ, 668, 182
Reich, W. 1982, A&AS, 48, 219
Reich, P., & Reich, W. 1986, A&AS, 63, 205
Reich, P., Testori, J. C., & Reich, W. 2001, A&A, 376, 861
Rice, W. 1993, AJ, 105, 67
Rieke, G. H., Young, E. T., Engelbracht, C. W., et al. 2004, ApJS, 154, 25
Rosset, C., Tristram, M., Ponthieu, N., et al. 2010, A&A, 520, A13
Sauvage, M., & Thuan, T. X. 1992, ApJ, 396, L69
Shetty, R., Kauffmann, J., Schnee, S., Goodman, A. A., & Ercolano, B. 2009, ApJ, 696, 2234
Silsbee, K., Ali-Haïmoud, Y., & Hirata, C. M. 2011, MNRAS, 411, 2750
Smith, M. W. L., Eales, S. A., Gomez, H. L., et al. 2012, ApJ, 756, 40
Spitzer Science Center 2012, IRAC Instrument Handbook (v2.0.2), Tech. Rep., California Institute of Technology
Stansberry, J. A., Gordon, K. D., Bhattacharya, B., et al. 2007, PASP, 119, 1038
Stevens, J. A., Amure, M., & Gear, W. K. 2005, MNRAS, 357, 361
Strong, A. W., Orlando, E., & Jaffe, T. R. 2011, A&A, 534, A54
Tabatabaei, F. S., & Berkhuijsen, E. M. 2010, A&A, 517, A77
Tabatabaei, F. S., Berkhuijsen, E. M., Frick, P., Beck, R., & Schinnerer, E. 2013, A&A, 557, A129
Tauber, J. A., Mandolesi, N., Puget, J., et al. 2010, A&A, 520, A1
Taylor, J. E., Moodley, K., & Diego, J. M. 2003, MNRAS, 345, 1127
Temi, P., Brighenti, F., Mathews, W. G., & Bregman, J. D. 2004, ApJS, 151, 237
Tibbs, C. T., Paladini, R., & Dickinson, C. 2012, Adv. Astron., 2012, 124931
Todorović, M., Davies, R. D., Dickinson, C., et al. 2010, MNRAS, 406, 1629
Unwin, S. C. 1983, MNRAS, 205, 787
Valtchanov, I. 2014, The Spectral and Photometric Imaging Receiver (SPIRE) Handbook, v.2.5 (European Space Agency)
Viaene, S., Fritz, J., Baes, M., et al. 2014, A&A, 567, A71
Walterbos, R. A. M., & Greenawalt, B. 1996, ApJ, 460, 696
Walterbos, R. A. M., & Schwering, P. B. W. 1987, A&A, 180, 27
Werner, M. W., Roellig, T. L., Low, F. J., et al. 2004, ApJS, 154, 1
Wheelock, S., III, T. N. G., Chillemi, J., et al. 1994, IRAS Sky Survey Atlas Explanatory Supplement, http://irsa.ipac.caltech.edu/IRASdocs/issa.exp.sup/, JPL Publication 94-11
Xu, C., & Helou, G. 1996, ApJ, 456, 152
Zacchei, A., Maino, D., Baccigalupi, C., et al. 2011, A&A, 536, A5
Zhu, Y.-N., Wu, H., Cao, C., & Li, H.-N. 2008, ApJ, 686, 155

[1] APC, AstroParticule et Cosmologie, Université Paris Diderot, CNRS/IN2P3, CEA/lrfu, Observatoire de Paris, Sorbonne Paris Cité, 10 rue Alice Domon et Léonie Duquet, 75205 Paris Cedex 13, France
[2] Aalto University Metsähovi Radio Observatory and Dept of Radio Science and Engineering, PO Box 13000, 00076 Aalto, Finland
[3] African Institute for Mathematical Sciences, 6–8 Melrose Road, Muizenberg, 7945 Cape Town, South Africa
[4] Agenzia Spaziale Italiana Science Data Center, via del Politecnico snc, 00133 Roma, Italy
[5] Aix Marseille Université, CNRS, LAM (Laboratoire d'Astrophysique de Marseille) UMR 7326, 13388 Marseille, France
[6] Astrophysics Group, Cavendish Laboratory, University of Cambridge, J J Thomson Avenue, Cambridge CB3 0HE, UK
[7] Astrophysics & Cosmology Research Unit, School of Mathematics, Statistics & Computer Science, University of KwaZulu-Natal, Westville Campus, Private Bag X54001, 4000 Durban, South Africa
[8] Atacama Large Millimeter/submillimeter Array, ALMA Santiago Central Offices, Alonso de Cordova 3107, Vitacura, 763 0355 Casilla, Santiago, Chile
[9] CITA, University of Toronto, 60 St. George St., Toronto ON M5S 3H8, Canada
[10] CNRS, IRAP, 9 Av. colonel Roche, BP 44346, 31028 Toulouse Cedex 4, France
[11] California Institute of Technology, Pasadena CA 91125, California, USA
[12] Centro de Estudios de Física del Cosmos de Aragón (CEFCA), Plaza San Juan 1, planta 2, 44001 Teruel, Spain
[13] Computational Cosmology Center, Lawrence Berkeley National Laboratory, Berkeley, CA 94720 California, USA
[14] DSM/Irfu/SPP, CEA-Saclay, 91191 Gif-sur-Yvette Cedex, France
[15] DTU Space, National Space Institute, Technical University of Denmark, Elektrovej 327, 2800 Kgs. Lyngby, Denmark
[16] Département de Physique Théorique, Université de Genève, 24 Quai E. Ansermet, 1211 Genève 4, Switzerland
[17] Departamento de Astrofísica, Universidad de La Laguna (ULL), 38206 La Laguna, Tenerife, Spain
[18] Departamento de Física, Universidad de Oviedo, Avda. Calvo Sotelo s/n, 33003 Oviedo, Spain
[19] Department of Astrophysics/IMAPP, Radboud University Nijmegen, PO Box 9010, 6500 GL Nijmegen, The Netherlands
[20] Department of Physics & Astronomy, University of British Columbia, 6224 Agricultural Road, Vancouver, British Columbia, Canada
[21] Department of Physics and Astronomy, Dana and David Dornsife College of Letter, Arts and Sciences, University of Southern California, Los Angeles, CA 90089, USA
[22] Department of Physics and Astronomy, University College London, London WC1E 6BT, UK
[23] Department of Physics, Florida State University, Keen Physics Building, 77 Chieftan Way, Tallahassee, Florida, USA
[24] Department of Physics, Gustaf Hällströmin katu 2a, University of Helsinki, 00100 Helsinki, Finland

[25] Department of Physics, Princeton University, Princeton, NJ 08544 New Jersey, USA
[26] Department of Physics, University of California, Santa Barbara, California, USA
[27] Department of Physics, University of Illinois at Urbana-Champaign, 1110 West Green Street, Urbana, Illinois, USA
[28] Dipartimento di Fisica e Astronomia G. Galilei, Università degli Studi di Padova, via Marzolo 8, 35131 Padova, Italy
[29] Dipartimento di Fisica e Scienze della Terra, Università di Ferrara, via Saragat 1, 44122 Ferrara, Italy
[30] Dipartimento di Fisica, Università La Sapienza, P.le A. Moro 2, 00185 Roma, Italy
[31] Dipartimento di Fisica, Università degli Studi di Milano, via Celoria, 16 Milano, Italy
[32] Dipartimento di Fisica, Università degli Studi di Trieste, via A. Valerio 2, 34128 Trieste, Italy
[33] Dipartimento di Fisica, Università di Roma Tor Vergata, via della Ricerca Scientifica, 1 Roma, Italy
[34] Discovery Center, Niels Bohr Institute, Blegdamsvej 17, Copenhagen, Denmark
[35] European Southern Observatory, ESO Vitacura, Alonso de Cordova 3107, Vitacura, 19001 Casilla, Santiago, Chile
[36] European Space Agency, ESAC, Planck Science Office, Camino bajo del Castillo, s/n, Urbanización Villafranca del Castillo, 28692 Villanueva de la Cañada, Madrid, Spain
[37] European Space Agency, ESTEC, Keplerlaan 1, 2201 AZ Noordwijk, The Netherlands
[38] Facoltà di Ingegneria, Università degli Studi e-Campus, via Isimbardi 10, 22060 Novedrate (CO), Italy
[39] Gran Sasso Science Institute, INFN, viale F. Crispi 7, 67100 L'Aquila, Italy
[40] HGSFP and University of Heidelberg, Theoretical Physics Department, Philosophenweg 16, 69120 Heidelberg, Germany
[41] Haverford College Astronomy Department, 370 Lancaster Avenue, Haverford, Pennsylvania, USA
[42] Helsinki Institute of Physics, Gustaf Hällströmin katu 2, University of Helsinki, 00100 Helsinki, Finland
[43] INAF–Osservatorio Astrofisico di Catania, via S. Sofia 78, Catania, Italy
[44] INAF–Osservatorio Astronomico di Padova, Vicolo dell'Osservatorio 5, 35141 Padova, Italy
[45] INAF–Osservatorio Astronomico di Roma, via di Frascati 33, Monte Porzio Catone, 00136 Roma, Italy
[46] INAF–Osservatorio Astronomico di Trieste, via G.B. Tiepolo 11, 34131 Trieste, Italy
[47] INAF/IASF Bologna, via Gobetti 101, 40127 Bologna, Italy
[48] INAF/IASF Milano, via E. Bassini 15, 20133 Milano, Italy
[49] INFN, Sezione di Bologna, Via Irnerio 46, 40126 Bologna, Italy
[50] INFN, Sezione di Roma 1, Università di Roma Sapienza, Piazzale Aldo Moro 2, 00185 Roma, Italy
[51] INFN/National Institute for Nuclear Physics, via Valerio 2, 34127 Trieste, Italy
[52] Imperial College London, Astrophysics group, Blackett Laboratory, Prince Consort Road, London, SW7 2AZ, UK
[53] Infrared Processing and Analysis Center, California Institute of Technology, Pasadena, CA 91125, USA
[54] Institut Universitaire de France, 103 Bd Saint-Michel, 75005 Paris, France
[55] Institut d'Astrophysique Spatiale, CNRS (UMR 8617), Université Paris-Sud 11, Bâtiment 121, 91400 Orsay, France
[56] Institut d'Astrophysique de Paris, CNRS (UMR 7095), 98bis Boulevard Arago, 75014 Paris, France
[57] Institute for Space Sciences, Bucharest-Magurale, Romania
[58] Institute of Astronomy, University of Cambridge, Madingley Road, Cambridge CB3 0HA, UK
[59] Institute of Theoretical Astrophysics, University of Oslo, 0371 Blindern, Oslo, Norway
[60] Instituto de Astrofísica de Canarias, C/Vía Láctea s/n, La Laguna, 38205 Tenerife, Spain
[61] Instituto de Física de Cantabria (CSIC-Universidad de Cantabria), Avda. de los Castros s/n, 39005 Santander, Spain
[62] Istituto Nazionale di Fisica Nucleare, Sezione di Padova, via Marzolo 8, 35131 Padova, Italy
[63] Jet Propulsion Laboratory, California Institute of Technology, 4800 Oak Grove Drive, Pasadena, California, USA
[64] Jodrell Bank Centre for Astrophysics, Alan Turing Building, School of Physics and Astronomy, The University of Manchester, Oxford Road, Manchester, M13 9PL, UK
[65] Kavli Institute for Cosmology Cambridge, Madingley Road, Cambridge, CB3 0HA, UK
[66] Kazan Federal University, 18 Kremlyovskaya St., 420008 Kazan, Russia
[67] LAL, Université Paris-Sud, CNRS/IN2P3 Orsay, France
[68] LERMA, CNRS, Observatoire de Paris, 61 Avenue de l'Observatoire, 75014 Paris, France
[69] Laboratoire AIM, IRFU/Service d'Astrophysique – CEA/DSM – CNRS – Université Paris Diderot, Bât. 709, CEA-Saclay, 91191 Gif-sur-Yvette Cedex, France
[70] Laboratoire Traitement et Communication de l'Information, CNRS (UMR 5141) and Télécom ParisTech, 46 rue Barrault, 75634 Paris Cedex 13, France
[71] Laboratoire de Physique Subatomique et Cosmologie, Université Grenoble-Alpes, CNRS/IN2P3, 53 rue des Martyrs, 38026 Grenoble Cedex, France
[72] Laboratoire de Physique Théorique, Université Paris-Sud 11 & CNRS, Bâtiment 210, 91405 Orsay, France
[73] Lawrence Berkeley National Laboratory, Berkeley, California, USA
[74] Lebedev Physical Institute of the Russian Academy of Sciences, Astro Space Centre, 84/32 Profsoyuznaya st., Moscow, GSP-7, 117997, Russia
[75] Max-Planck-Institut für Astrophysik, Karl-Schwarzschild-Str. 1, 85741 Garching, Germany
[76] McGill Physics, Ernest Rutherford Physics Building, McGill University, 3600 rue University, Montréal, QC, H3A 2T8, Canada
[77] National University of Ireland, Department of Experimental Physics, Maynooth, Co. Kildare, Ireland
[78] Nicolaus Copernicus Astronomical Center, Bartycka 18, 00-716 Warsaw, Poland
[79] Niels Bohr Institute, Blegdamsvej 17, 2100 Copenhagen, Denmark
[80] Optical Science Laboratory, University College London, Gower Street, London WC1E GBT, UK
[81] SISSA, Astrophysics Sector, via Bonomea 265, 34136 Trieste, Italy
[82] School of Physics and Astronomy, Cardiff University, Queens Buildings, The Parade, Cardiff, CF24 3AA, UK
[83] Sorbonne Université-UPMC, UMR 7095, Institut d'Astrophysique de Paris, 98bis Boulevard Arago, 75014 Paris, France
[84] Space Sciences Laboratory, University of California, Berkeley, CA 90095 California, USA
[85] Special Astrophysical Observatory, Russian Academy of Sciences, Nizhnij Arkhyz, Zelenchukskiy region, 369167 Karachai-Cherkessian Republic, Russia
[86] Sterrewacht Leiden, Leiden University, PO Box 9513, 2300 RA Leiden, The Netherlands
[87] Sub-Department of Astrophysics, University of Oxford, Keble Road, Oxford OX1 3RH, UK
[88] UK ALMA Regional Centre Node, Jodrell Bank Centre for Astrophysics, Alan Turing Building, School of Physics and Astronomy, The University of Manchester, Oxford Road, Manchester, M13 9PL, UK
[89] UPMC Univ. Paris 06, UMR7095, 98bis Boulevard Arago, 75014 Paris, France
[90] Université de Toulouse, UPS-OMP, IRAP, 31028 Toulouse Cedex 4, France
[91] University of Granada, Departamento de Física Teórica y del Cosmos, Facultad de Ciencias, 18071 Granada, Spain
[92] University of Granada, Instituto Carlos I de Física Teórica y Computacional, 18071 Granada, Spain
[93] Warsaw University Observatory, Aleje Ujazdowskie 4, 00-478 Warszawa, Poland